

Dongxu WU, Fengzhou FANG

Development of surface reconstruction algorithms for optical interferometric measurement

© The Author(s) 2021. This article is published with open access at link.springer.com and journal.hep.com.cn

Abstract Optical interferometry is a powerful tool for measuring and characterizing areal surface topography in precision manufacturing. A variety of instruments based on optical interferometry have been developed to meet the measurement needs in various applications, but the existing techniques are simply not enough to meet the ever-increasing requirements in terms of accuracy, speed, robustness, and dynamic range, especially in on-line or on-machine conditions. This paper provides an in-depth perspective of surface topography reconstruction for optical interferometric measurements. Principles, configurations, and applications of typical optical interferometers with different capabilities and limitations are presented. Theoretical background and recent advances of fringe analysis algorithms, including coherence peak sensing and phase-shifting algorithm, are summarized. The new developments in measurement accuracy and repeatability, noise resistance, self-calibration ability, and computational efficiency are discussed. This paper also presents the new challenges that optical interferometry techniques are facing in surface topography measurement. To address these challenges, advanced techniques in image stitching, on-machine measurement, intelligent sampling, parallel computing, and deep learning are explored to improve the functional performance of optical interferometry in future manufacturing metrology.

Keywords surface topography, measurement, optical interferometry, coherence envelope, phase-shifting algorithm

1 Introduction

The functional performance of a workpiece is greatly influenced by its surface topography, including surface form and surface texture. Surface topography carries the significant traces of its manufacturing process, varying from traditional manufacturing, such as cutting, grinding, and polishing, to advanced and nontraditional manufacturing techniques, such as diamond turning [1], magnetorheological finishing [2], plasma polishing [3], and additive manufacturing [4]. Obtaining highly accurate and repeatable surface measurements of the workpiece is critical for the process of quality control, design improvement, and final product acceptance [5]. Surface metrology is a fundamental and indispensable part of precision manufacturing, whose broad applications can be found in various areas, such as optics [6–8], precision engineering [9–11], tribology and corrosion [12], microelectromechanical systems (MEMS) [13,14], and biomedical applications [15,16]. Effective measurement and evaluation of surface topography for the precision manufacturing process is becoming more important than ever because modern science and technology place higher demands on high-tech components with complex shapes and high accuracy. For example, freeform components with a nanometric surface finish and submicron form accuracy can greatly improve optical performance and reduce system size [17]. However, performing accurate measurements of the freeform surface in a conventional measuring device is extremely challenging due to the lack of axis of rotational invariance.

Currently, a variety of surface metrology methods and instruments have been developed for various application prospects. As shown in Table 1, on the basis of different

Received April 28, 2020; accepted July 16, 2020

Dongxu WU, Fengzhou FANG (✉)
Centre of Micro/Nano Manufacturing Technology (MNMT-Dublin),
University College Dublin, Dublin 4, Ireland
E-mail: fengzhou.fang@ucd.ie

Dongxu WU
School of Control Engineering, Northeastern University at Qinhuangdao,
Qinhuangdao 066004, China

Fengzhou FANG
State Key Laboratory of Precision Measuring Technology and
Instruments, Centre of Micro/Nano Manufacturing Technology
(MNMT), Tianjin University, Tianjin 300072, China

measuring principles [18–22], surface metrology instruments can vary from contact-type stylus profilometers [23] to near-contact atomic force microscope (AFM) [24] and to non-contact optical instruments [5]. Among the developed metrology techniques, optical interferometry offers notable advantages, including non-contact mode, high accuracy, high resolution, and well-defined traceability route to the definition of meter [25]. Optical interferometry is capable of 3D areal surface topography measurements with sub-nanometric accuracy, attracting much attention from both academia and industry.

Although the optical interferometry techniques have gained widespread use in various areas, some problems and challenges need to be solved urgently in practical applications. First, most commercial optical interferometers can conduct surface measurement appropriately in a well-controlled environment but cannot be applicable to manufacturing sites, where the measurement process suffers from environmental noise and mechanical vibration. Some on-machine measurement instruments based on optical interferometry have been developed to address this problem [26–29]. In this way, surface measurement can be implemented on the machine tool or even in the manufacturing process without removing or remounting the workpiece [30,31]. Second, implementing the fewest measurements with the highest possible speed and accuracy is always desirable but also challenging. The fringe analysis algorithm is an essential part of surface

topography reconstruction from digitized interferograms. Algorithms with high accuracy, good robustness and performance are always computationally intensive, thereby making them unsuitable for real-time applications. Third, aside from the limitation on the lateral resolution, surface discontinuities and high slopes may degrade fringe contrast, which is why the measurement of complex micro/nanostructured surfaces remains a challenging task. Therefore, fast and accurate measurement of precision components with complex shapes and extremely tight tolerances, such as freeform optics and roller mold, is still in urgent demand and continues to be an active area of research. In addition to the support of auxiliary fiducials or adjustable fixtures [7], designing intelligent and robust algorithms is more important to increase measurement availability and efficiency.

This paper presents a comprehensive overview of surface reconstruction algorithms for optical interferometric measurements. Even though some good review papers have been written on this topic [5,25,32,33], this paper stands out because it provides an advanced perspective on optical interferometric techniques from a manufacturing point of view. Detailed and in-depth descriptions of measurement principles, fringe analysis, and surface reconstruction for different measurement requirements are given. Theoretical background and recent advances for various fringe analysis algorithms are extensively considered. The major challenges facing the

Table 1 Comparison of commercially available surface metrology instruments

No.	Measurement principle	Commercial instrument	Performance	Applications or accessible samples
1	Stylus profilometry	Form Talysurf [®] PGI Optics [18]	Gauge range: Up to 28 mm; noise: < 2 nm <i>Rq</i> ; measurement area: Up to 300 mm diameter; form error: < 100 nm	Plastic lenses; small components; diffractive optics; infrared glass and crystals
2	AFM	Bruker's Dimension Icon [19]	<i>X-Y</i> scan range: 90 μm × 90 μm; <i>Z</i> range: 10 μm; <i>X-Y</i> position noise: ≤ 0.15 nm RMS; <i>Z</i> sensor noise: 35 pm RMS; sample size: ≤ 210 mm diameter; sub-nanometer resolution	Surface imaging; surface roughness; atomic mica lattice; carbon nanotubes
3	Optical interferometry	Zygo NewView [™] 9000 [20]	Manual <i>XY</i> : 100 mm travel; motorized <i>XY</i> : 150 mm travel; tilt: ±4° tilt; repeatability: 0.08 nm for all magnifications; sub-nanometer vertical resolution	Materials characterization; MEMS; semiconductor; consumer electro-optics; optical surface manufacturing
4	Confocal scanning	LEXT OLS5000 [21]	Field of view: 16–5120 μm; height resolution: 0.5 nm; lateral resolution: 0.12 μm; repeatability (50×): 0.012 μm; measurement noise: 1 nm	Inner texture; fuel injector nozzle; bearing ball; ultrasonic transducer; micro needle
5	LVDT probe	Moore Nanotech's Workpiece Error Compensations System [22]	Air bearing; miniature; accuracy of the probe: < 25 nm; slopes: Up to 60° per side; desired form accuracy (after correction): 0.05–0.15 μm	On-machine part geometry measurement and form error correction

Abbreviations. *Rq*: Root mean square deviation; AFM: Atomic force microscope; RMS: Root mean square; MEMS: Micro-electromechanical systems; LVDT: Linear variable differential transformer.

interferometric measurement of surface topography are presented. Finally, the paper forecasts future research opportunities and discusses the feasibility of some emerging techniques as a means of improving the measurement performance of optical interferometers.

2 Major optical interferometry techniques

Optical interferometry is recognized as one of the most effective and reliable techniques for surface topography measurement in many areas. Optical interferometric techniques and related instruments have been continuously developed and may be categorized according to various criteria. To systematize the interferometric techniques used in the manufacturing field, this paper focuses on surface topography measurement and divides the major techniques into four different categories.

2.1 Phase-shifting interferometry

Unlike the classical analysis of static interferograms that suffers from errors in finding the fringe centers [34], phase-shifting interferometry (PSI) overcomes such limitation by collecting a series of interferograms (normally at least three) with controlled phase shift. The intensity data of the interferograms contain the information of the wavefront phase in the variations, which can be recorded by the image sensor to recover the phase. Phase modulation can be achieved by a variety of means, such as a rotating polarizer, a moving diffraction grating, a tilted glass plate, and a moving mirror [35]. Even though PSI can achieve full 3D images with sub-nanometric height repeatability, its dynamic range is limited. The single-wavelength PSI is suitable only for the cases where the difference of optical path difference (OPD) between two adjacent data points is less than $1/2$ wavelength (λ) [36]. To be specific, if the slope of the measured surface changes steeply, then height ambiguities of multiples of half wavelengths will occur [37]. The 2π ambiguity problem limits the PSI technique to be used only to measure relatively smooth and continuous surfaces [38,39]. To overcome the slope limitation, one can use two shorter wavelengths to synthesize a longer equivalent wavelength [40]. Hence, two-wavelength techniques can effectively increase the dynamic measurement range of PSI without introducing the 2π ambiguity [41–43].

Two-wavelength PSI can be used to correct the 2π ambiguity. However, the calculated phase data for the equivalent wavelength has larger noise and error amplitude, especially for steeper surface topography. To overcome the error amplification effect, the phase data of a third wavelength can be introduced to perform more correction steps to enhance the capability of two-wavelength PSI [36]. Furthermore, multi-wavelength PSI has been developed to increase the range of unambiguity in step height

measurement [44]. As shown in Fig. 1, Warnasooriya and Kim [45] developed a light emitting diode (LED)-based multi-wavelength phase imaging interference microscopy to increase the unambiguous axial range without increasing phase noise. The measurement range of the single-wavelength PSI has been extended by taking multiple measurements based on two or more shorter visible wavelengths [46–48], but these techniques are still unsatisfactory due to the limited depth of focus of the objective [49]. White-light PSI (WLPSI) can avoid the phase ambiguity problem [50]. The spectrally resolved white-light interferometer is helpful to determine the phase-shift error [51], but this requires more complicated data processing and longer computation times.

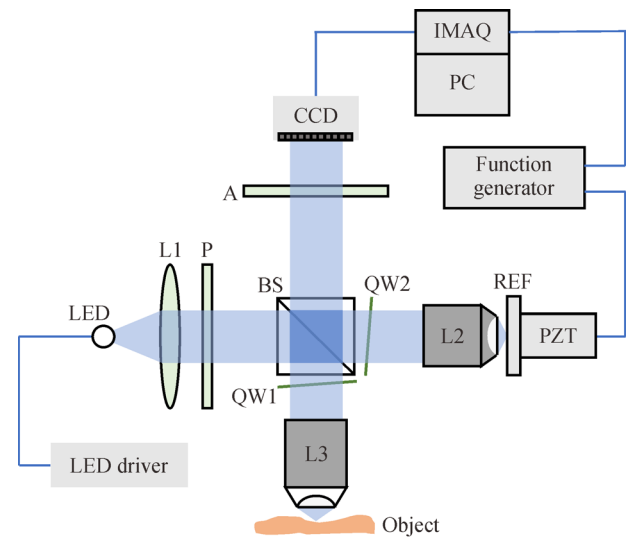


Fig. 1 Schematic of LED-based multi-wavelength phase imaging interference microscopy. L1: Collimating lens; L2 and L3: Microscope objectives; P: Polarizer; A: Analyzer; CCD: Charge coupled device; IMAQ: Image acquisition board; PC: Personal computer; LED: Light emitting diode; BS: Beam splitter; QW1 and QW2: Quarter wave plates; PZT: Piezoelectric transducer; REF: Reference mirror. Adapted with permission from Ref. [45]. © The Optical Society.

2.2 Coherence scanning interferometry

PSI is capable of non-contact areal surface topography measurements with high accuracy and resolution, but it often suffers from inherent 2π ambiguity, insufficient wavelength accuracy, and environmental instability [52]. Profilometers based on coherence scanning interferometry (CSI) can overcome the above limitations. In terms of the working principle, CSI monitors the interference fringe contrast rather than detecting the interference phase. CSI is also referred to as scanning white-light interferometry (SWLI) [53] or vertical scanning interferometry (VSI) [54]. Low-coherence white light is advantageous for obtaining high contrast interference fringes when the

OPD between a test surface and a reference surface approaches zero because of the large spectral bandwidth of the source [55]. The surface heights can be determined by seeking the scanning position where the fringe contrast is at the maximum. Alternatively, the positions of zero OPD along the optical axis represent the surface heights under test [56].

A scanning actuator such as a piezoelectric transducer (PZT) drives the interference objective to make continuous motion along the vertical axis, which synchronizes the scan of focus and optical path length [32]. Figure 2 [57] shows a typical layout of CSI using a Linnik objective. The sample is placed on a motorized axial translation stage to perform a single vertical scan. The peak positions of the fringe envelope along the scanning direction are measured, which corresponds to the height of the surface [57,58]. To achieve the accurate zero OPD position, Zhou et al. [59] employed a laser Michelson interferometry system to calibrate the displacement of the PZT stage in an SWLI system.

CSI can suppress spurious interference from scattered light and is suitable for the measurement of discontinuous or rough surfaces [60]. Therefore, CSI has gradually become one of the most common techniques in optical interferometers for surface topography measurement. Based on multiple reflection phenomena, a micro-V-groove dihedral measurement method that uses white light interferometry (WLI) was proposed [61]. Despite the attractiveness of this method, the major limitation of CSI is that using the loci of points, where a maximum fringe contrast for mapping surface topography exists, requires an enormous amount of measurements and computations for each point. The fringe contrast calculation based on the sparse discrete sampling is not accurate enough. A smaller

sampling interval or interpolation method would bring more computation burden. One can adopt advanced computing techniques to rapidly retrieve the fringe envelope. Another problem is that the fringe contrast calculation highly depends on the wavelength of the light source and the fidelity of the scanning stage. The measurement accuracy may deteriorate quickly due to changes in illumination strength or environmental conditions, as well as the distortions of the fringe envelope shape [62].

2.3 Wavelength scanning interferometry

Even though the VSI overcomes the 2π phase ambiguity and extends the application range of optical interferometers [63,64], it must be performed with a mechanical scanning of a probe head or the specimen stage, which limits its measurement speed [54,65]. Unlike VSI, wavelength scanning interferometry (WSI) can perform absolute surface height measurement without any mechanical scanning [66,67]. The fundamental principle of WSI is to derive the OPD between the reference light and the object light by the wavelength scanning of a tunable laser [68–71]. The measurement based on WSI relies on wavelength variations to achieve phase shifts without introducing any 2π phase ambiguity. A fast and environmentally robust surface measurement system based on WSI was proposed by Jiang et al. [72]. As shown in Fig. 3, this WSI system includes a measurement interferometer and a reference interferometer, and they share a common optical path and suffer from similar environmental noise. The environmental noise is compensated by the reference interferometer. As a key component of this system, the acousto-optic tunable filter (AOTF) is adopted to select a specific

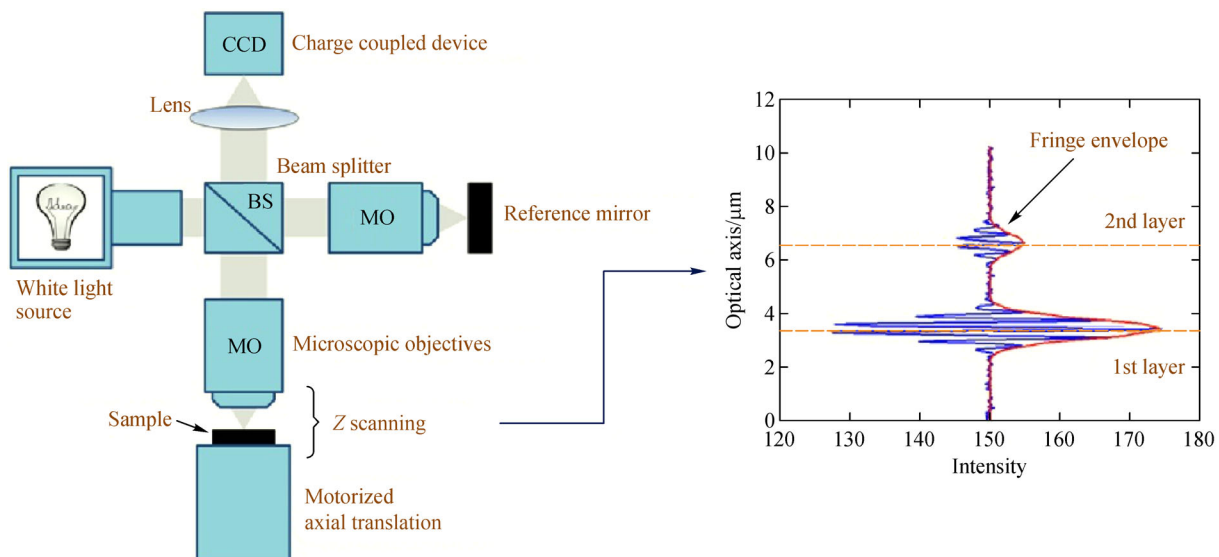


Fig. 2 Typical layout of CSI using a Linnik objective. BS: Beam splitter; MO: Microscope objectives; CCD: Charge coupled device. Adapted with permission from Ref. [57]. © The Optical Society.

wavelength to produce an interferogram. Particularly, AOTF has a resolution of 1–10 nm with a 30–400 μm coherence length.

WSI is suitable for real-time surface shape measurement [68], as it benefits from its distinct advantages of no mechanical scanning, fast measurement, and high resolution [73]. Gao et al. [74] developed a WSI system for surface and thickness measurement of a transparent film. Muhamedsalih et al. [75] described a parallel programming method to accelerate the computing analysis in surface measurement with the compensation of environmental noise. Moschetti et al. [76] achieved unambiguous surface height measurements with improved repeatability. A dual-probe WSI for double-sided near-right-angle structured surfaces has also been proposed in Ref. [77].

WSI is widely accepted to be able to perform accurate surface topography measurements in a well-controlled working environment. However, it is still vulnerable to environmental disturbance, such as temperature fluctuations, mechanical vibrations, and air disturbances. To address these issues, the fringe algorithm optimization based on an adaptive filter has been reported to improve measurement accuracy and immunity to environmental noise [78].

2.4 Heterodyne interferometry

One weakness of the homodyne technique (e.g., PSI and

CSI) is that the interference fringe resulting from a weak measurement light and a strong reference light has poor visibility, typically when the reflectivity of the test surface is low. The heterodyne technique has been developed for high-sensitivity surface profile measurements using a high-speed scanning stage to achieve the Doppler frequency shift [79]. However, the measurement accuracy of the heterodyne interferometer is limited by the mechanical instability of the scanning stage when performing the frequency shifting.

Heterodyne interferometer generally adopts a common-path configuration to reduce the environmental turbulence [80,81]. The Zeeman-split laser is conventionally used to output two common-path polarized beams, but the Zeeman difference frequency is typically limited to 3–4 MHz, which also suffers from the anisotropic effects of the laser cavity [82,83]. An acousto-optic modulator (AOM) can be employed to avoid nonorthogonality and elliptic polarizations [84,85]. Matsumoto et al. [86,87] adopted two spherical mirrors to compensate for the diffraction angles on different wavelengths due to the AOM. To improve the measurement resolution and accuracy of WSI, Dai and Katuo [88] developed a wavelength scanning heterodyne interferometer by combining a high-resolution heterodyne phase measurement with a wide span of the frequency scanning. The optical heterodyne interferometer with a common-path configuration can effectively eliminate the phase noise and is insensitive to environmental

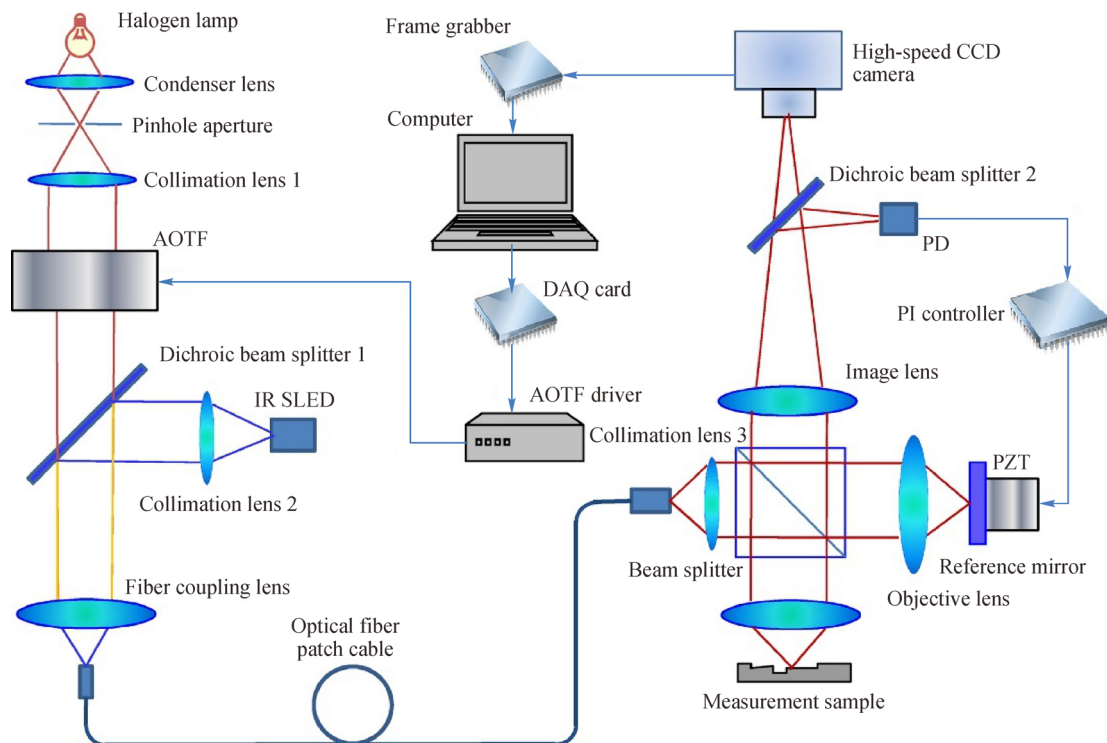


Fig. 3 Schematic of WSI with compensation of environmental noise. AOTF: Acousto-optic tunable filter; IR SLED: Near-infrared superluminescent light-emitting diode; DAQ: Data acquisition card; CCD: Charge coupled device; PD: Photodiode; PZT: Piezoelectric transducer. Adapted with permission from Ref. [72]. © The Optical Society.

disturbance. However, heterodyne interferometry (HI) is more demanding in terms of system hardware than PSI and CSI, requiring a larger detector bandwidth and more optical components.

A variety of optical interferometric techniques and instruments have been developed to conduct surface topography measurements. Table 2 summarizes the state-of-the-art research [89–95] on various interferometric techniques and corresponding specifications and applications. Recently, some novel interferometric techniques, such as diffraction phase microscopy [96,97] and quantitative phase imaging [98], have been proposed for nanoscale surface topography measurement. Considering the strong requirements, optical interferometric techniques will continue to attract researchers' attention to further improve their operability, capability, and flexibility.

3 Theory of fringe analysis algorithms

Fringe analysis algorithms are essential for optical interferometric measurements to effectively reconstruct the surface topography. Even though a variety of fringe analysis algorithms have been developed over a wide range of application areas [33,99–101], the performance of an algorithm is affected by many factors [102]. The selection of an appropriate fringe analysis algorithm needs trade-off considerations because the desired measurement accuracy, speed, resolution, and robustness vary depending on the algorithms [103]. Over the past decades, great efforts in surface metrology have resulted in the development of many algorithms for reconstructing surface topography. A comparison of different fringe analysis algorithms in active use is given in this section.

The existing fringe analysis algorithms discussed below can be divided into two broad categories. One is to calculate the envelope center of the interference fringes to obtain the accurate position of zero OPD from the discrete intensity data points [49,99,104–106], such as coherence peak sensing (CPS) [54]. The other is to extract the phase information of the central wavelength of the interference fringes by Fourier transform (FT) [107–109] and phase-shifting method [110,111]. Thus, the surface topography can be achieved based on the envelope phase retrieval.

3.1 Centroid approach

The broad-bandwidth interference fringes are approximately symmetrical about the zero OPD. The light intensity received by the detector varies in amplitude corresponding to different OPD, and a coherence peak is present at the position of zero OPD [112]. The coherence peaks at different scanning position z represent different surface heights. The value of z corresponding to the peak of the modulation function $f(z)$ is also equivalent to the centroid of the function that is naturally used to estimate the position of the coherence peak. Ai and Novak [113] proposed a centroid approach for estimating the modulation peak in broad-bandwidth interferometry. The relationship between the scanning position z where a modulation peak exists and the modulation function $f(z)$ was determined as

$$z = \frac{\sum [zf(z)]}{\sum f(z)}. \quad (1)$$

The central fringe nearest to the centroid position can be identified from its adjacent fringes [114]. If the function

Table 2 Comparison of current optical interferometry techniques

Principle	Method	Measurement range (z)	Vertical resolution	Measurement speed	Repeatability	Samples under test
PSI	Profiling [36]; Areal [43,89,90]	OPD between two adjacent data points is less than $\lambda/2$ [36]; 7.84 μm unambiguous range [45]	Several nanometers [45]; 1/1000 of a fringe [91]	0.39 s for 10 interferograms at a resolution of 480 \times 640 pixels [92]	2.5 nm RMS [36]; 0.5 nm RMS [90]	Off-axis parabola [36]; stepped surface [43]; biological cells [45]; micro-sphere [89]; fused silica [90]
CSI	Areal [49,53,56,61]	Over a dynamic range of 10 μm [57]; 100 μm [53]	Sub-nanometer [53]	8 s for 20 μm step height [53]; 115 s for two 10 μm step heights [93]	0.5 nm [53]	Machined steel [49]; 921 nm-high grating [53]; etched silicon [56]; wavy transparent layer [57]; micro V-groove [61]
WSI	Areal [72,74,76,77]	200 μm [72]; $\pm 120 \mu\text{m}$ [76]	Nanometric scale [77]	0.42 s for 128 captured frames [75]; 1.25 s for $\pm 120 \mu\text{m}$ z -heights [76]	Sub-nanometer [76]	Stepped surface [72]; transparent film [74]; semiconductor daughterboard [75]; metallized prismatic film [77]
HI	Profiling [87,94]; Areal [95]	27 μm [94]	0.31 nm [82]; 0.2 nm [94]	0.2 μm scanning speed of PZT [86]	0.5 nm [94]	Semiconductor [82]; stepped surface [87]; corneal surface profile [95]

Abbreviations. PSI: Phase-shifting interferometry; OPD: Optical path difference; RMS: Root mean square; CSI: Coherence scanning interferometry; WSI: Wavelength scanning interferometry; HI: Heterodyne interferometry; PZT: Piezoelectric transducer.

$f(z)$ is not perfectly symmetrical, then a shift of z will consistently repeat during scanning. The square of the first-order derivative of the interference signal is a converging function that has a centroid repetitively close to the position of the coherence peak. Therefore, a more accurate calculation of the value of z corresponding to the position of the coherence peak could be achieved by the following equation [113]:

$$z = \frac{\sum \{z[I(z) - I(z - \Delta z)]^2\}}{\sum [I(z) - I(z - \Delta z)]^2}, \quad (2)$$

where $I(z)$ is the interferometric signal, and Δz denotes the scanning step in the time domain.

The centroid approach is capable of determining surface height directly from the digitized interferograms by estimating the envelope peak. The systematic error of the centroid can be eliminated by setting the aperture in the lens [115]. This approach is simple and computationally economical, thereby being suitable for fast surface topography measurement. However, the centroid is comparatively sensitive to environmental noise, especially at a large sampling interval. The centroid position may not be necessarily consistent with the envelope peak if noise is present in the correlogram [116], resulting in some false information in the obtained fractional phase.

3.2 Fourier transform

FT is an effective mathematical tool for processing digital interferograms [107,117]. FT method for phase demodulation has been extensively adopted in surface profile measurement since it was introduced by Takeda et al. [118,119], taking the advantages of single-shot nature, full-field analysis, and high precision [120]. In a Mirau interferometer, the interference fringes result from the cross correlation of the signals reflected from the reference mirror and the test surface [121]. If the test surface is focused, then the OPD between the reference beam and the measuring beam will be zero. Otherwise, the OPD will increase significantly. Consequently, the cross correlation of these two signals captured by the charge coupled device (CCD) camera decreases sharply due to the low-coherence light source. The output signal from the CCD camera ($I(x, y, z)$) can be given as follows [122]:

$$I(x, y, z) = A^2(x, y) + B^2 + 2A(x, y)B\gamma[z - z_0(x, y)], \quad (3)$$

where (x, y) are spatial coordinates, $A(x, y)$ and B are the amplitudes of the signals reflected from the sample and reference mirror, respectively, corresponding to the background bias. The term $\gamma(x, y, z)$ can be approximated by an envelope function $g[z - z_0(x, y)]$ with a maximum at $z = z_0(x, y)$. Hence, the correlation term (I_{AB}) in Eq. (3) can be expressed as [122]

$$I_{AB} = 2A(x, y)B\gamma[z - z_0(x, y)]\cos\{\varphi[(z - z_0(x, y))]\}, \quad (4)$$

where $\varphi[(z - z_0(x, y))]$ indicates a phase variation. Fast FT (FFT) is capable of extracting the phase and the envelope from the term I_{AB} . After one forward transform of the profile data in the z direction, the negative-frequency components can be eliminated, and the packet of the positive-frequency components can be recentered. Finally, one inverse transform is carried out to obtain the demodulated correlation function that can be written as [122]

$$I_{AB}^d = 2A(x, y)B\gamma[z - z_0(x, y)]\exp\{i\varphi[z_0(x, y)]\}. \quad (5)$$

The phase in Eq. (5) corresponds to the surface profile height $z_0(x, y)$. The aforementioned method can be used to obtain the envelope peak. However, it is computationally intensive because the image data in each pixel need to be filtered in the frequency domain through one forward transform and one inverse transform. Even if great progress has been made, the computational efficiency and accuracy of the FFT method of determining the envelope peak are still attracting wide attention.

3.3 Windowed Fourier transform

FT has been regarded as a complex and inaccurate method because of its global property [123]. As a local approach, windowed FT (WFT) is a simple and more robust method for fringe pattern processing [124,125]. Kemao et al. [126,127] introduced two-dimensional WFT for fringe demodulation based on two algorithms: Windowed Fourier filtering (WFF) and windowed Fourier ridges (WFR). WFT and inverse WFT can be expressed as [128]

$$Sf(u, \xi) = \int_{-\infty}^{\infty} f(x)w(x-u)\exp(-j\xi x)dx, \quad (6)$$

$$f(x) = \frac{1}{2\pi} \int_{-\infty}^{\infty} \int_{-\infty}^{\infty} Sf(u, \xi)w(x-u)\exp(j\xi x)d\xi du, \quad (7)$$

where u is the translated coordinate, $w(x)$ is a window function, ξ is the frequency center, and j is the imaginary unit. The window function $w(x)$ can be chosen as a Gaussian function, which is the main difference between the two transform pairs. As WFT is carried out in a local area, the WFT spectrum $Sf(u, \xi)$ presents not only the spectrum components but also the location where a component happens in the time domain [128].

3.4 Hilbert transform

Hilbert transform (HT) shares a similar working principle with the FT method. However, HT is more flexible in terms of computational efficiency and accuracy [129]. Chim and Kino [130] proposed an HT algorithm for reconstructing a three-dimensional surface profile with a low-cost frame

grabber. The frequency response $H(e^{j\omega})$ of the HT can be given by [130]

$$H(e^{j\omega}) = \begin{cases} -j, & 0 \leq \omega < \pi, \\ j, & \pi \leq \omega < 2\pi, \end{cases} \quad (8)$$

where $\omega = 2\pi k_z \Delta z$ denotes the angular frequency, k_z and Δz are the spatial frequency and step size of the PZT driver, respectively. If the background bias ($A^2(x,y) + B^2$) in Eq. (3) is removed from the input image $I_{xy}(n)$, then an unbiased image $i_{xy}(n)$ is obtained and the demodulation function ($V_{xy}(n)$) can be written as [130]

$$V_{xy}(n) = i_{xy}(n) + j i_{xy}^*(n), \quad (9)$$

where $i_{xy}^*(n)$ indicates the $\pi/2$ phase-shifted image from $i_{xy}(n)$. The normalized impulse response $h_{\text{norm}}(n)$ for HT with $(2M+1)$ elements can be given by [130]

$$h_{\text{norm}}(n) = \begin{cases} \frac{1}{n} & \text{if } |n| \leq M \text{ and } n \text{ is odd,} \\ 0, & \text{otherwise} \end{cases} \quad (10)$$

where M is an odd integer. Hence, the phase-shifted image $i_{xy}^*(n)$ can be expressed as the convolution of $i_{xy}(n)$ with $h_{\text{norm}}(n)$ and can be simplified into the following form [130]

$$i_{xy}^*(n) = \frac{2}{\pi} \sum_{\substack{m=1 \\ m \text{ is odd}}}^M \frac{i_{xy}(m-n) - i_{xy}(m+n)}{m}. \quad (11)$$

Therefore, the amplitude and phase of the function $V_{xy}(n)$ can be calculated based on the known phase-shifted image $i_{xy}^*(n)$, as described by Eq. (11). The simplicity of the normalized impulse response $h_{\text{norm}}(n)$ means that the algorithm based on HT allows a greater reduction in computation time than other algorithms that have to work pixel by pixel. HT is thus a promising technique for performing real-time imaging [131]. A two-dimensional interferometric phase can also be demodulated using the discrete HT with the raster scanning procedure [132].

3.5 Wavelet transform

As shown in Eqs. (3) and (4), the intensity distribution of the interferogram is expressed as a cosine-modulated function. The interference signal processing can thus be considered as detecting a cosine-modulated function simultaneously in both time and frequency domains. Wavelet transform (WT) is an effective method for processing non-constant signals by time–frequency analysis. WT algorithms have already been widely used in the demodulation of white-light interferograms [104,105,133].

Given its greatest similarity to the interferogram, the Morlet wavelet is chosen as the mother wavelet that can be written as [134]

$$\psi(z) = \frac{1}{\sqrt{\pi f_b}} e^{i2\pi f_c z} e^{-(z^2/f_b)}, \quad (12)$$

where f_b represents the bandwidth of the mother wavelet, and f_c represents its center frequency. One-dimensional continuous WT (CWT) of the interferogram $I(z)$ can be expressed as [134,135]

$$W_I(a,b) = \int_{-\infty}^{\infty} I(z) \psi_{a,b}^*(z) dz, \quad (13)$$

$$\psi_{a,b}(z) = \frac{1}{\sqrt{a}} \psi\left(\frac{z-b}{a}\right), \quad (14)$$

where $\psi_{a,b}(z)$ denotes a complete set of daughter wavelets, in which a , corresponding to the frequency domain, indicates the scaling factor that controls the wavelet compression or dilation, and b , corresponding to the spatial domain, indicates the shift factor that controls the temporal translation. $*$ indicates the complex conjugate. The argument and modulus of the correlation coefficient $W_I(a,b)$ give the phase and modulus of the interferogram $I(z)$ [104,136]. The interference signals are scanned along the temporal direction by using the daughter wavelets with different frequencies. The maximum correlation coefficient between the signals and wavelets can be achieved to determine the frequency and peak position, respectively [133].

3.6 Frequency domain analysis

Fringe contrast methods have been widely used in 3D surface profiling, facilitating the widespread application of white-light interferometers, but the noise in fringes can cause the positions of the envelope peak to be incorrectly determined [62]. In 1994, Deck and de Groot [53,137] proposed a frequency domain analysis (FDA) method for processing the white-light interferograms to reconstruct a 3D surface profile without relying on fringe contrast. A white-light interferogram can be regarded as a sum of a series of single-wavelength interference fringes due to the incoherent superposition. The phase information of single-wavelength interference fringes is recovered by performing FT of the interferogram. Surface heights are thus obtained based on the calculated phase. A single-wavelength interference fringe in space can be expressed as a series of sinusoidal functions, whose interferometric phase ϕ is related to the OPD Z by [62]

$$\phi = kZ, \quad (15)$$

where $k = 2\pi/\lambda$ denotes the angular wavenumber of the light source. Hence, the white-light interferograms possess a sequence of wavenumbers, each corresponding to a single interferogram that is incoherently superimposed to the others to generate the final white-light interferograms. The phase of each separate interferogram as a function of

wavenumber can be written in the form of a Taylor series expansion [62]

$$\phi = k_0 Z_0 + (k - k_0) G_0 + \frac{(k - k_0)^2}{2} \left. \frac{dG}{dk} \right|_{k_0} + \dots, \quad (16)$$

where k_0 denotes the mean wavenumber, and G denotes the group velocity OPD. For $k = k_0$, G_0 is given by [62]

$$G_0 = Z_0 + k \left. \frac{dZ}{dk} \right|_{k_0}. \quad (17)$$

The unknown information in Eq. (16) can be recovered from the function of the phase with respect to the wavenumber, which can be obtained from the interference function $I(Z_i)$ by performing discrete FT. For a particular wavenumber k_j , the j th component of the FT ($P(k_j)$) can be written as [62]

$$P(k_j) = \sum_i I(Z_i) e^{-ik_j Z_i}, \quad (18)$$

where Z_i denotes the equally-spaced OPD position. Therefore, the amplitude $A(k_j)$ and desired phase $\phi(k_j)$ as a function of the wavenumber k_j can be given by

$$A(k_j) = |P(k_j)|, \quad (19)$$

$$\phi(k_j) = \arg\{P(k_j)\}. \quad (20)$$

Therefore, a series of pairs $\{\phi(k_j), k_j\}$ are acquired from the region where the amplitude $A(k_j)$ is the maximum for calculating the parameters in Eq. (16). Subsequently, fringe order in high-precision phase data is resolved correctly using the FDA [138]. A signal model for a low-coherence interferometer is established by performing the superposition sum in the frequency domain [139].

The FDA offers some remarkable features such as excellent repeatability and a high scanning rate [62], because the entire interferogram data is processed and utilized in the spatial-frequency domain. Consequently, FDA is computationally intensive and requires a powerful signal processing system.

3.7 Phase-shifting algorithms

Phase-shifting algorithm (PSA) originates from the phase measurement method in a classical laser interferometry technique, which requires multiple (at least three) frames of fringe intensity data to reconstruct the 3D surface profile. The phase of a wavefront is encoded in the intensity variations of the recorded interferograms. The wrapped phase and intensity modulation can be demodulated from the phase-shifted interferograms to obtain the height values of the sample surface at each point. The light intensity of a two-beam interference fringe can be given approximately by [35]

$$I(z) = I_0 \{1 + M(z) \cos[\phi(z)]\}, \quad (21)$$

where I_0 indicates a constant background intensity, $M(z)$ indicates the fringe visibility (also called modulation), and $\phi(z)$ is the wavefront phase.

3.7.1 Three-step algorithm

Three-step PSA is a preferable choice because a minimum of three fringe images are needed to reconstruct 3D surface topography, reducing the measurement time. If the phase shifts of $-2\pi/3$, 0 , and $2\pi/3$ are chosen, then the light intensities of the three fringe images ($I_1(z)$, $I_2(z)$, and $I_3(z)$) can be respectively expressed as [140]

$$\begin{cases} I_1(z) = I_0 \{1 + M(z) \cos[\phi(z) - 2\pi/3]\}, \\ I_2(z) = I_0 \{1 + M(z) \cos[\phi(z)]\}, \\ I_3(z) = I_0 \{1 + M(z) \cos[\phi(z) + 2\pi/3]\}. \end{cases} \quad (22)$$

The wavefront phase $\phi(z)$ and intensity modulation $M(z)$ at each pixel can be calculated by

$$\phi(z) = \arctan \frac{\sqrt{3}(I_1(z) - I_3(z))}{2I_2(z) - I_1(z) - I_3(z)}, \quad (23)$$

$$M(z) = \frac{\sqrt{3(I_1(z) - I_3(z))^2 + (2I_2(z) - I_1(z) - I_3(z))^2}}{I_1(z) + I_2(z) + I_3(z)}. \quad (24)$$

Only the phase value in the range of $[-\pi, \pi]$ can be obtained by Eq. (23). The phase ambiguities need to be removed by a phase unwrapping algorithm to reconstruct the continuous phase map. The surface height can be achieved by determining the frame position with the maximum intensity modulation $M(z)$.

3.7.2 Five-step algorithm

Hariharan et al. [141] proposed an error-compensating phase calculation algorithm using five measurements of the intensity, which could tolerate relatively greater errors than the three-step algorithm. Larkin [99] improved Hariharan's algorithm and first introduced the PSA into the white-light interferogram processing. If the phase step between frames is $\pi/2$, then the wavefront phase $\phi(z)$ and intensity modulation $M(z)$ at each pixel can be calculated by [99]

$$\phi(z) = \arctan \frac{\sqrt{4(I_2(z) - I_4(z))^2 - (I_1(z) - I_5(z))^2}}{2I_3(z) - I_1(z) - I_5(z)}, \quad (25)$$

$$\begin{aligned} M^2(z) &\propto (I_2(z) - I_4(z))^2 - (I_1(z) - I_3(z)) \\ &\quad \times (I_3(z) - I_5(z)), \end{aligned} \quad (26)$$

where $I_1(z)$ to $I_5(z)$ represents the five consecutive fringe intensities measured for each pixel. When the modulation is at its maximum, the height of the sample surface that is directly linked to the best-focus scanning-frame position can be expressed as [54]

$$z(x,y) = \Delta z N + \frac{f}{2} \frac{(\Delta z \phi + 2l\pi)\bar{\lambda}}{2\pi}, \quad (27)$$

where Δz denotes the step size, N denotes the step number, f denotes the numerical aperture (NA) factor of the interference objective, l denotes the fringe order that has to be determined in the phase-unwrapping process, and $\bar{\lambda}$ denotes the mean wavelength.

The computational efficiency of Larkin's method is two to three times better than that of the HT technique. Under random noise with a standard deviation of 2% of the modulation value, the position error in the step size of the five-step algorithm is 6.4%, which is better than that of the Fourier–Hilbert algorithm and envelope centroid method [99].

3.7.3 Seven-step algorithm

For the three-step and five-step algorithms, the background intensity and the fringe visibility must be assumed to be constant during recording the fringe intensities. In this case, the introduced phase shift is considered to be the only factor that causes variations in fringe intensities. But in practice, the fringe visibility varies with the OPD due to the coherence envelope. Under the assumption of local linearity of the coherence envelope, the wavefront phase $\phi(z)$ and intensity modulation $M(z)$ based on a seven-step algorithm can be expressed as [50,142]

$$\phi(z) = \arctan \frac{3I_3(z) + I_7(z) - I_1(z) - 3I_5(z)}{4I_4(z) - 2I_2(z) - 2I_6(z)}, \quad (28)$$

$$\begin{cases} M(z) = \frac{3I_3(z) + I_7(z) - I_1(z) - 3I_5(z)}{\sin\phi(z)}, & \sin\phi(z) > \cos\phi(z), \\ M(z) = \frac{4I_4(z) - 2I_2(z) - 2I_6(z)}{\cos\phi(z)}, & \sin\phi(z) \leq \cos\phi(z), \end{cases} \quad (29)$$

where $I_1(z)$ to $I_7(z)$ represent the seven consecutive fringe intensities with a phase step of $\pi/2$.

The seven-step algorithm is capable of compensating for the variation in the fringe visibility and performing exact phase measurements without 2π ambiguities. Moreover, the seven-step algorithm has excellent resistance to the distortions in the phase shift and low-frequency mechanical vibration [109,143]. However, ensuring that the central intensity $I_4(z)$ is recorded within the zero-order fringe during the data acquisition procedure is difficult. Therefore, the absolute phase measurement cannot be

guaranteed [50]. The seven-step algorithm involves more data frames to suppress errors, which is why computational efficiency is also a concern.

4 Recent advances in fringe analysis algorithms

4.1 Improvement of measurement accuracy and repeatability

In recent years, many research efforts have gone into developing novel fringe analysis methods with desired features such as high estimation accuracy and repeatability. In VSI, the discontinuity of the measured surface may cause the fringe modulation envelope to skew and the peak position to shift away when the coherence length of the white-light source is larger than the step height [116]. To obtain the accurate position of the maximum fringe contrast, Vo et al. [93] combined the WLPSI and FFT algorithms to determine the local fringe peak. As shown in Fig. 4, the proposed algorithm can achieve nanometric vertical resolution with satisfactory repeatability and stability when measuring the step height. Dong and Chen [144] proposed an advanced FT analysis method to eliminate the spectrum leakage issue and the edge error, but it was more time-consuming because this algorithm required FFT to be performed multiple times. Ma et al. [145] employed the WFT method to retrieve the phase of a white-light interferogram and correct the position of zero OPD, but the speed of the proposed algorithm should be further improved. Least-square estimation using the short-time FT has been utilized to retrieve more accurate envelope peak of the white-light interferogram and the corresponding phase values simultaneously [146]. Even though WFT is a more appropriate method to retrieve the wrapped phase during measuring objects with discontinuities and/or large slopes, it is more computationally intensive than the FT method [147].

The multi-resolution property of WT in the time-frequency domains improves the vertical resolution of the interferometric measurement. Li et al. [134] clarified the phase and the modulus of the WT coefficients at the ridge position under two kinds of daughter wavelet definitions, verifying the correctness and accuracy of the wavelet ridge techniques. The 2D WT approach has been developed to calculate the modulation of the fringe patterns in measuring the complex and step-like surfaces [148]. Serizawa et al. [149] employed the CWT method to achieve high accuracy in the 3D surface profile measurement without linear interpolation of the acquired fringe.

The early PSAs are restricted by computational limits. With the major improvements of computer and information science in interferometric metrology, the number of image frames has advanced from 3 to 5, 7, and even 15 frame varieties [150]. Currently, PSAs with more flexibility,

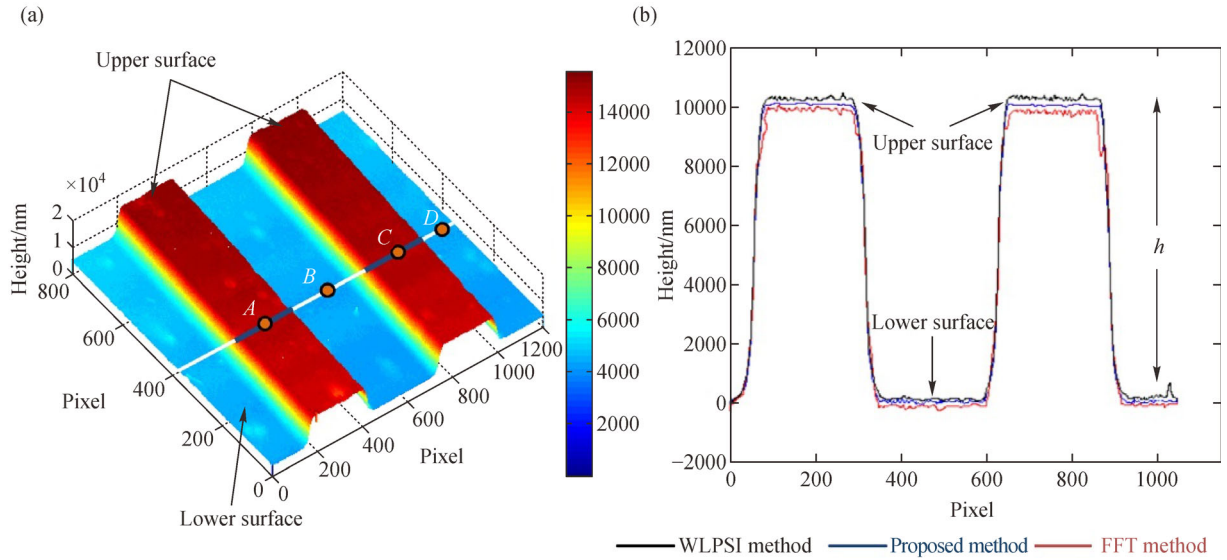


Fig. 4 Measurement of the two continuous standard step heights: (a) 3D plot of a reconstructed two continuous 10 μm standard step heights and (b) comparison of 2D profiles obtained by the three methods. WLPsi: White-light phase-shifting interferometry; FFT: Fast Fourier transform. Adapted with permission from Ref. [93]. © The Optical Society.

higher accuracy and speed are increasingly desirable for suppressing environmental noise and system errors. de Groot [150] derived a 101-frame algorithm that is highly resistant to error sources, but this very long PSA is not practical because the calibration error would cause a sudden decline in signal strength. Deck [90] reduced the spectral overlap of PSI induced by the tuning nonlinearity through combining a high-precision wavelength monitor and an FT. WLPsi can overcome the 2π ambiguity and provide high resolution. Shen et al. [151,152] pointed out that the measurement results based on the higher-step PSAs were more repeatable than those of traditional five- and seven-step PSAs, as shown in Fig. 5. The highest applicable step of PSA is limited by the fringe resolving ability of the optical system. The increased number of the possible phase-determining functions is thus a real challenge.

4.2 Noise resistance

As a major challenge for fringe analysis, unexpected measurement noise may significantly disturb the outcome of data acquisition and deteriorate the measurement accuracy. Fringe analysis algorithms with high noise resistance are always desired in the practical application of interferometric instruments. The CWT method is more tolerant to signal noise and more accurate in determining local fringe peak than the global methods such as FT [153] because CWT can effectively average out the noise. Wei et al. [154,155] pointed out that the position of the envelope peak could be obtained by using only the spectral signals with a high signal-to-noise ratio (SNR) rather than all frequency components of the signals.

Pavliček and Michalek [156] investigated the influence of the noise of the interferogram on the measurement uncertainty by means of HT. The envelope noise can be correlated, and its correlation function relies on the sampling step and the mean wavelength of the light source. When the envelope peak is extracted by using the HT algorithm, the background term needs to be eliminated primarily from the interferogram. However, two interferograms that are acquired successively often have slightly different background illuminations induced by environmental disturbances and different scanning positions due to the NA of the objective. Thus, precisely subtracting the background term from the interferograms is difficult. Huang et al. [157] developed a new algorithm for analyzing nonlinear and non-stationary data, designated as the Hilbert–Huang transform (HHT). Trusiak et al. [158,159] employed HHT to achieve efficient adaptive filtering and accurate phase demodulation by using local fringe direction estimation. As shown in Fig. 6, the dynamic microbead profile provided by the single-shot Hilbert–Huang phase microscopy (S2H2PM) is smoother and has a more cone-like structure than the one retrieved using the FT approach [160]. Therefore, as an empirical approach, the developed algorithms based on the HHT are suitable for a wide variety of interference fringes acquired in an environment with noise and inconstant contrast and background, ensuring their applicability to dynamic measurements [161,162].

It is hardly possible for an algorithm to deal with a small number of phase-shifted interferograms with strong noise and small interval. Deng et al. [163] constructed a set of connected interferograms by means of simple subtraction and addition operations between interferograms to retrieve

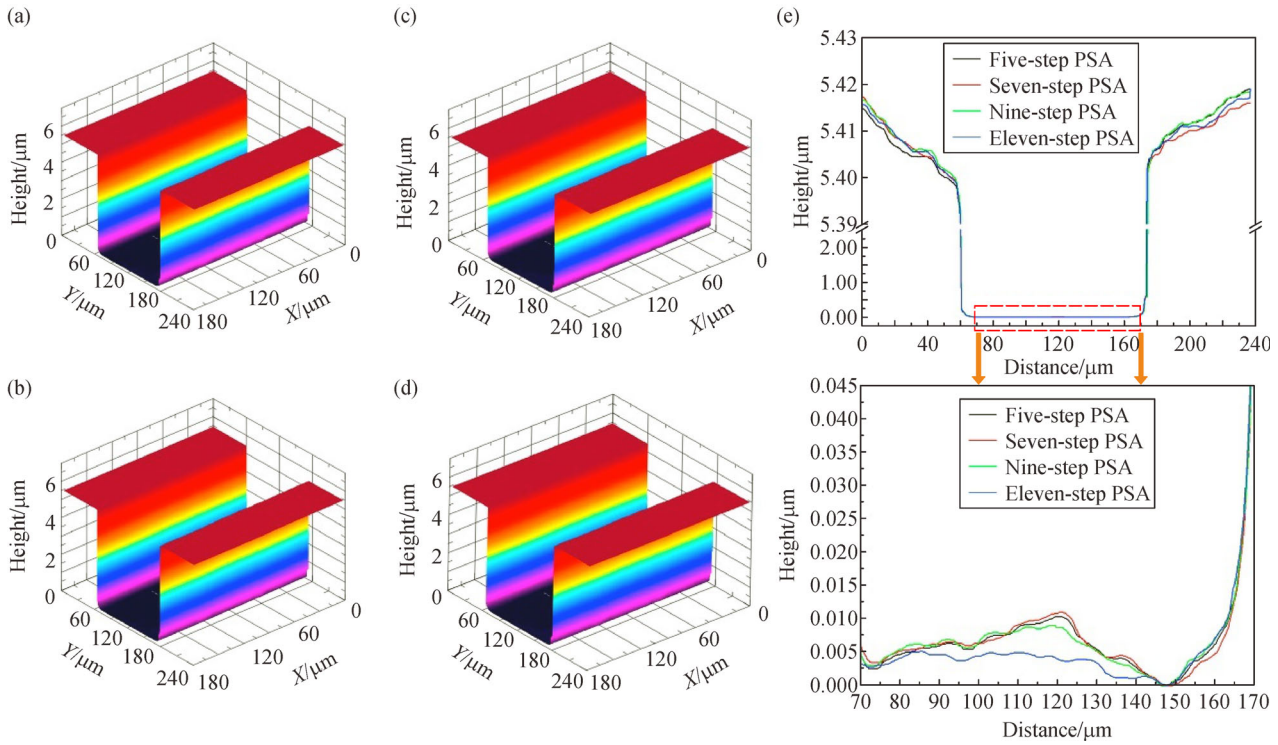


Fig. 5 Measurement results of the test object using four PSAs: (a) Five-step phase-shifting, (b) seven-step phase-shifting, (c) nine-step phase-shifting, (d) eleven-step phase-shifting, and (e) cross section of the test object. PSA: Phase-shifting algorithm. Reproduced from Ref. [152] with permission from Elsevier.

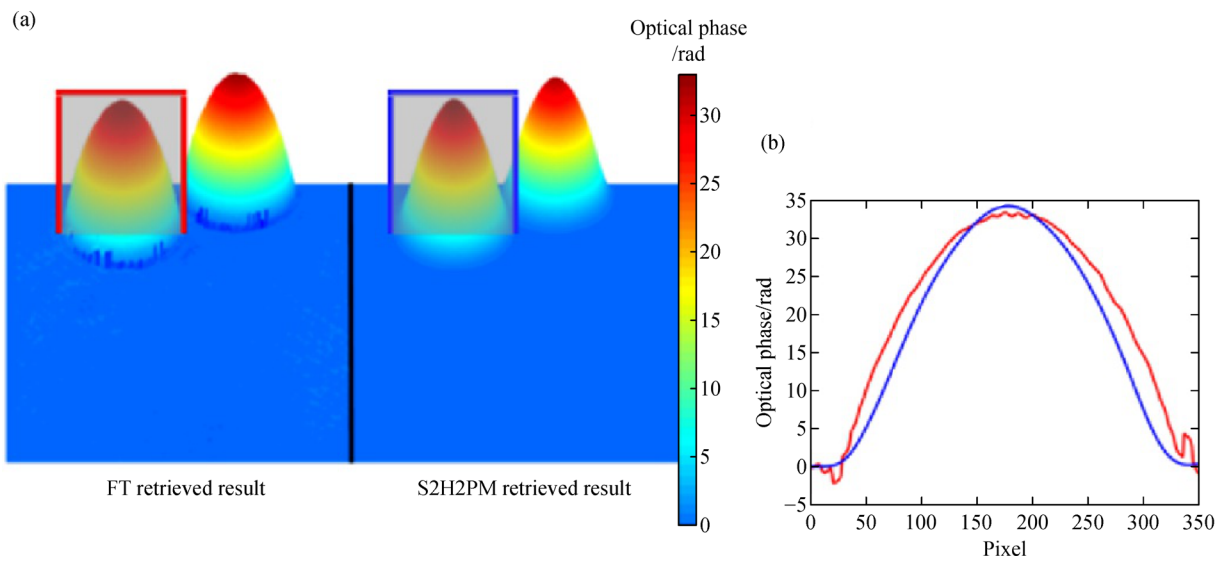


Fig. 6 Measurement results for microbeads: (a) 3D plot phase distributions retrieved using dynamic S2H2PM and FT techniques and (b) phase cross sections of the same microbead by FT (red) and S2H2PM (blue) techniques. S2H2PM: Single-shot Hilbert–Huang phase microscopy; FT: Fourier transform. Adapted with permission from Ref. [160]. © The Optical Society.

the phase map under harsh conditions. Local polynomial phase approximation allows reliable phase estimation from a single fringe pattern and offers high robustness against severe noise without the need for complex unwrapping operations [164–166].

Unlike phase-shifting techniques, the spatial phase-demodulation methods, such as FT, WFT, and WT, are insensitive to noise because phase retrieval at each pixel depends on other pixels in the fringe pattern. However, these options offer poor performance around discontinuous

and isolated regions in the phase map [167]. In CSI, topography averaging and signal oversampling are two effective measurement noise reduction methods. However, the averaging method is incapable of extracting more surface information from the weak reflected lights. The oversampling method provides the benefit of capturing weak signals, but it has little effect on random noise, and its noise reduction ability weakens when handling surfaces with high slopes and roughness or a tilted flat surface [168].

4.3 High-speed fringe analysis

Fringe analysis algorithms need to be as accurate and as fast as possible when reconstructing the surface topography on an existing instrument. Gdeisat et al. [169] proposed a fast phase demodulation method using finite impulse response Hilbert transformers without depending on the specific fringe patterns or on the optical fringe projection system. Zhong et al. [170] pointed out that the WT method was capable of reconstructing the measured object with more details than the FT method that may smooth the measured surface, but the WT method would cost more time. Bernal et al. [171] presented a bespoke WT algorithm for measuring arbitrarily shaped vibrations by using two distinct mother wavelets to distinguish self-mixing fringe patterns and the displacement direction. However, the number of scales needed to be further optimized in real-time measurement. Gianto et al. [57] evaluated different types of envelope detection techniques and believed that CWT and Teager–Kaiser energy operator (TKEO) provided a better surface extraction than HT and five-sample adaptive method. In addition, TKEO outperformed CWT in terms of computation time.

On the basis of local polynomial phase approximation and subsequent state-space formulation, Rajshekhara and Rastogi [172] conducted phase estimation by using a single frame with a low computational burden and nonrequirement of 2D unwrapping operations. Recurrence computational algorithms have been applied to fringe analysis to increase the computational power and processing speed [173].

The WFT methods have been widely used for fringe analysis in various applications, but these methods are computationally intensive. A fast parallel WFT-based algorithm using graphics processing unit (GPU) has proven effective for real-time applications [174]. Rapid measurement of displacement derivatives of a deformed object is a challenging task. Recently, this problem has been addressed by the application of an efficient GPU-based Wigner–Ville distribution method [175]. The applicability of GPU-assisted diffraction phase microscopy has also been demonstrated for dynamic deformation testing in terms of reliability and computational efficiency [176].

4.4 Phase error compensation and correction

As one of the fairly common techniques for precise quantitative measurement of surface topography, PSI has drawn much attention from researchers. However, the accuracy of phase retrieval in PSI is susceptible to systematic errors. The common sources of systematic errors may be divided into two categories: Phase-shift error and non-sinusoidal waveform of the signal [177]. The coupling error of the phase-shift increment and harmonic distortions in the interference signal is widely overlooked. Phase-shift tuning errors can increase the sensitivity of PSAs to second-order and higher harmonics [178]. A 13-sample PSA for surface shape measurement of a transparent sample was designed, which could compensate not only for the phase-shift errors but also for the coupling errors between higher harmonics and phase-shift error [179]. On the basis of the least-squares iterative algorithm, Xu et al. [89] developed a dual-wavelength iterative method to compensate for the phase-shift errors, and the wrapped phases were accurately retrieved from dual-wavelength interferograms with arbitrary phase shifts and second-order harmonics. Figure 7 shows the measurement result of the spherical cap, whose peak-to-valley (PV) error and root mean square (RMS) error are less than 11.3 and 4.7 nm, respectively.

Advanced iterative algorithm (AIA) is capable of analyzing random phase-shifted interferograms with intra- and inter-frame intensity variations [180,181]. Conventional iterative algorithms are time consuming. To suppress random phase-shifting errors, Zhai et al. [92] proposed a non-iterative phase extraction algorithm based on Lissajous figures and ellipse fitting, and average phase-shift errors of less than 0.0055 rad for straight interferograms were achieved. Cai et al. [182,183] presented a four-frame algorithm for correcting the wavefront errors caused by arbitrary and unequal phase shift errors in PSI. Kim et al. [100] proposed a phase error correction algorithm of WLPSI using the average of the phase errors near the modulation peak. After the correction, a repeatability of 0.2 nm was obtained for a step height of 500 nm. The unknown phase shifts from only three phase-shifting interferograms can be extracted if the amplitude of the reference wave is approximately uniform [184]. To correct the phase-shifting error, Zhang et al. [185] developed a wavelength scanning digital holographic microscope (WS-DHM). As shown in Fig. 8, this WS-DHM is superior to WLI, confocal laser scanning microscopy (CLSM), and AFM in the measurement of micro pyramids with a 45° slope.

4.5 Self-calibration algorithms

Miscalibration error of the phase shifter may seriously reduce the measurement accuracy. Self-calibration PSAs

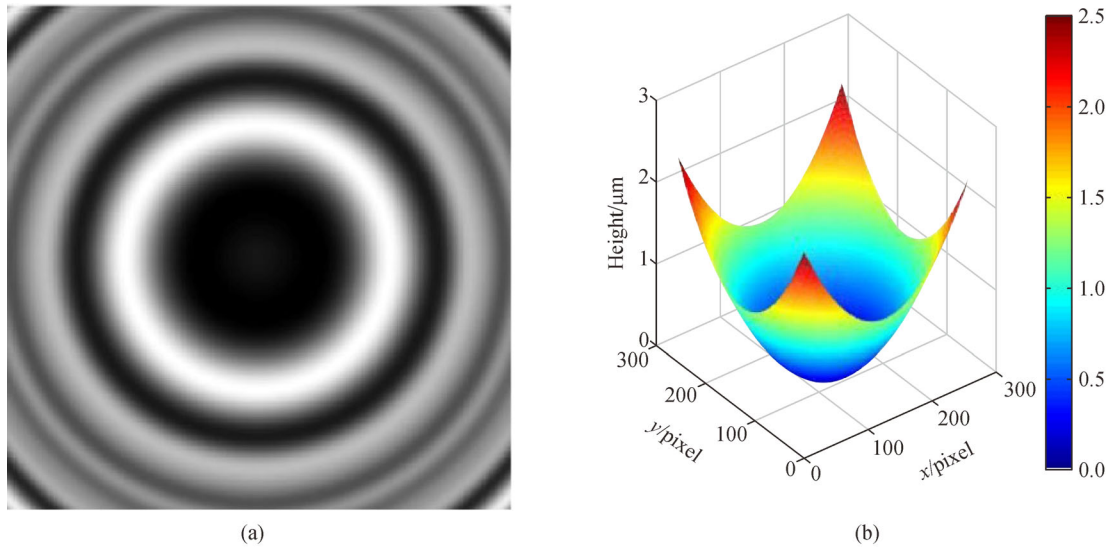


Fig. 7 Measurement of the spherical cap in the case of fringe number $\alpha = 0.4$: (a) One dual-wavelength interferogram containing the second-order harmonics and (b) the calculated height with the proposed method. Reproduced from Ref. [89] with permission from Elsevier.

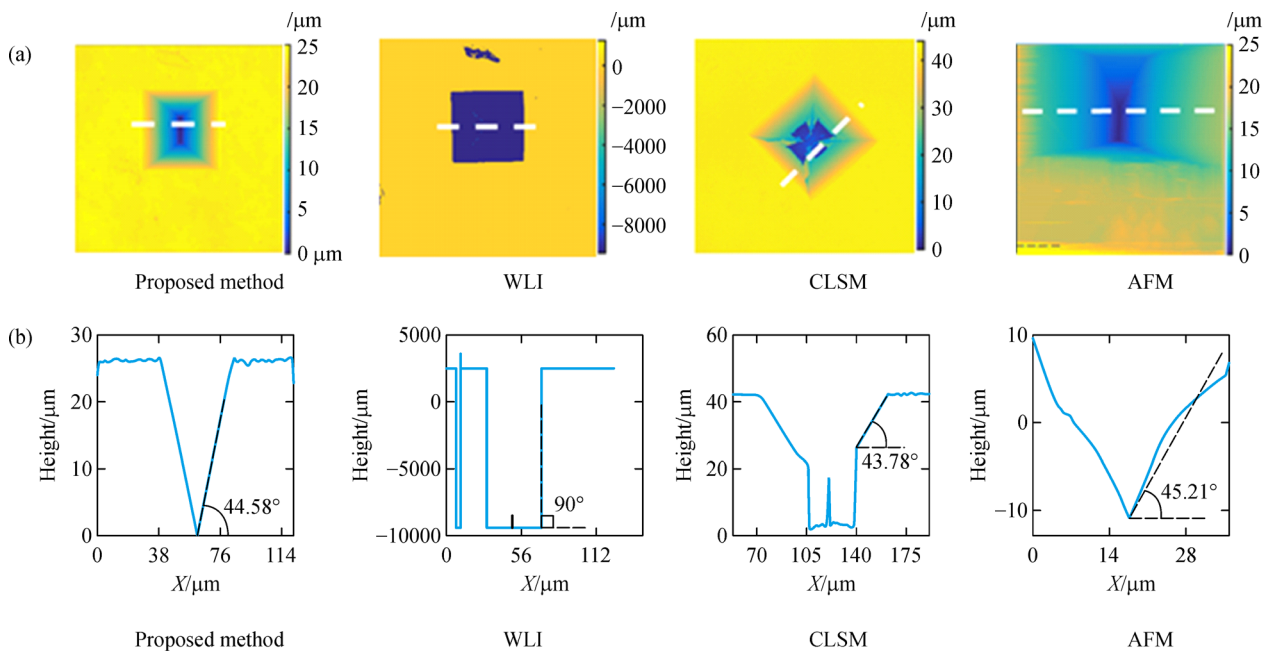


Fig. 8 Measurement results for the pyramid: (a) AFM images of the pyramid and (b) a cross section of the pyramid. WLI: White light interferometry; CLSM: Confocal laser scanning microscopy; AFM: Atomic force microscope. Reproduced from Ref. [185] with permission from IOP Publishing Ltd.

have been developed to solve this problem, and they require at least three interferograms for accurate phase retrieval [180,186]. However, the necessary assumption of the uniformities of the phase steps, amplitudes of the two interference beams, and background intensities is always not valid in practical measurements. Blind self-calibration PSAs based on a cross-bispectrum are capable of estimating the random phase shifts from only three fringe

patterns in the absence of any supplementary assumption [187,188].

Recently, Wang et al. [189] presented a novel self-calibration PSA called mid-band spatial spectrum matching (MSSM) to achieve phase retrieval from ultra-sparse fringe patterns (USFP). Figure 9 shows the measurement results using different algorithms. The RMS error of the phase retrieval using the MSSM algorithm is 0.024 rad,

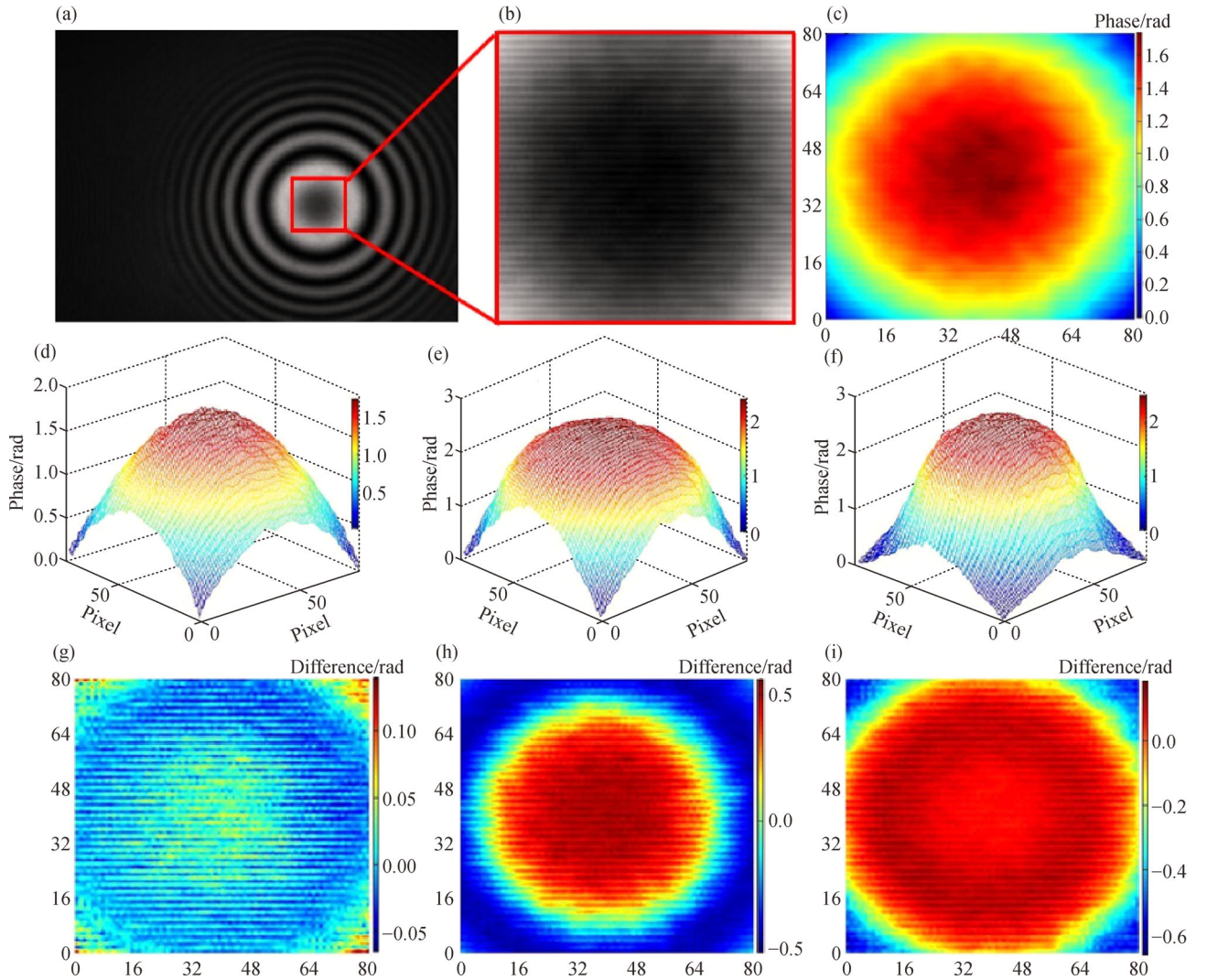


Fig. 9 Experimental results of USFP: (a) One-frame interferograms; (b) the intercepted USFP from (a); (c) the reference phase map of (b); (d) the retrieved phases by MSSM; (e) the retrieved phases by PCA; (f) the retrieved phases by AIA; the corresponding differences between the reference phase and the achieved phases by (g) MSSM, (h) PCA, and (i) AIA. USFP: Ultra-sparse fringe pattern; MSSM: Mid-band spatial spectrum matching; PCA: Principal component analysis; AIA: Advanced iterative algorithm. Adapted with permission from Ref. [189]. © The Optical Society.

outperforming principal component analysis (PCA) and AIA. The mid-frequency spatial spectrum of the fringe patterns can be employed to estimate the phase shift. However, the corresponding amplitude is always weak, and the accuracy of the phase retrieval is not assured when the fringe number in interferograms is less than one. On the basis of the spatial spectrum characters of the interferograms, Cao et al. [190] realized phase retrieval with strong self-calibration ability and ultra-high SNR. The proposed algorithm could process three-frame interferograms containing fewer than one fringe in the absence of strict temporal phase shifts.

As discussed above, recent advances have made fringe analysis algorithms even more attractive by providing

more satisfactory measurement results and better performance. The measurement performance and application of different types of fringe analysis algorithms are summarized in Table 3.

5 Challenges and perspective

As an effective means of surface profiling, optical interferometric technique has enjoyed tremendous popularity and notable development in various areas. Currently, topographical surface analysis with more variety and flexibility is increasingly needed in measurement and characterization of high-tech components, such as freeform

Table 3 Performance and applications of fringe analysis algorithms

No.	Author	Principle	Algorithm	Performance	Object	Remark
1	Ai and Novak [113]	VSI	Centroid method	Consistent repeatability even when the modulation function exhibited multiple peaks	3D surface topography	Free of the ambiguities in multi-peak modulation functions, suitable for rapid online applications
2	Dong and Chen [144]	Laser interferometer (Fizeau type)	FFT	Phase retrieval from a single-shot spatial carrier fringe pattern	Flat mirror	Highly efficient and timesaving for dynamic or real-time measurement
3	Vo et al. [93]	WLSI	FFT and PSA	Nanometric resolution and good repeatability	Step height; spherical surface	The batwing effects and positioning error in the maximum modulation were reduced
4	Ma et al. [145]	WLSI	WFT	Good noise immunity and a more accurate ZOPD position	CGH diffractive element	A smoothed and continuous profile of sharp step surface was obtained
5	Trusiak et al. [160]	Mach–Zehnder interferometry	HHT	Single-frame fast acquisition and processing time around 5–10 s	Static and flowing microbeads; red blood cells	Robust, fast, and accurate single-shot quantitative phase imaging for dynamic objects
6	Serizawa et al. [149]	SD-OCT	CWT	Measurement repeatability of 65.1 nm for 2D surface, RMS measurement error of 0.17 μm for 3D surface profile	Step height	High measurement accuracy without resampling the wavenumber or linear interpolation
7	de Groot and Deck [62]	WLSI	FDA	Measurement repeatability of 0.5 nm RMS, scanning rate of 2 $\mu\text{m/s}$	Sensing head; moth's eye	Without relying on fringe contrast, all data processing occurred in the spatial-frequency domain
8	Kim et al. [179]	Wavelength-tuning Fizeau interferometer	13-sample PSA	RMS phase error under 3 nm, even for a phase-shift miscalibration of $\pm 30\%$	Transparent fused silica plate	Compensation for miscalibration and first-order nonlinearity of phase shift, coupling errors, and bias modulation of intensity
9	Cao et al. [190]	Mach–Zehnder-type PSI	ASSF	RMS phase error less than 0.05 rad	Macrophage cell; light guide panel	Stable self-calibration phase retrieval with few interferograms containing fewer than one fringe

Abbreviations. VSI: Vertical scanning interferometry; FFT: Fast Fourier transform; WLSI: White-light scanning interferometry; PSA: Phase-shifting algorithm; WFT: Windowed Fourier transform; ZOPD: Zero optical path difference; CGH: Computer generated hologram; HHT: Hilbert–Huang transform; SD-OCT: Spectral domain optical coherence tomography; CWT: Continuous wavelet transform; RMS: Root mean square; WLSI: White-light scanning interferometry; FDA: Frequency domain analysis; PSI: Phase-shifting interferometry; ASSF: Advanced spatial spectrum fitting.

optics [6,191,192], highly reflective samples or transparent film [179,193], and micro/nanostructures [61,194,195]. Extensive developments and improvements have been made in data processing methods and accessible surface structures. Along with the recent advances, optical interferometric techniques are facing new challenges and emerging research opportunities in future surface metrology.

5.1 Challenges

5.1.1 Miscalibration error

The measurement accuracy of an optical interferometer fundamentally depends on the demodulation process of the underlying fringe phase information. Even though the PSAs are considered mathematically convenient and deterministic in the phase demodulation procedure, the error caused by the incorrect estimation of phase shifts is an inescapable problem [189,196]. PSAs adopt more than one phase-shifted fringe patterns (normally at least three)

to retrieve the phase information, providing the advantages of high resolution and accuracy in phase measurement. However, multiple-frame PSAs suffer from a limited dynamic measurement range and are sensitive to external disturbances and noise. The self-calibration ability in phase retrieval cannot be guaranteed if the phase-shifting interferograms contain fewer than one fringe. Low-noise phase retrieval from fewer interferograms with smaller phase shifts continues to be a challenge.

Currently, most calibration schemes rely on modeling methods or calibration references such as manufactured surfaces that are certified based on the ISO standards [32]. After these off-line calibration operations, the optical interferometers can achieve high measurement accuracy. However, the developed calibration instruments are typically expensive, and the complex calibration algorithms are computationally expensive and lack flexibility, thereby preventing their use in on-line or on-machine applications. Hence, the development of simple and accurate calibration algorithms is a key issue for extending the applications of optical interferometers.

5.1.2 Surface discontinuities and high slopes

Compared with PSAs, spatial phase-demodulation methods, such as FT [122,144], WFT [126,128] and WT [133,148], can retrieve the phase information from a single interferogram. The spatial phase calculation at each pixel is affected by the neighboring pixels or all pixels in the fringe patterns. Consequently, the spatial methods have better resistance to noise, but the accuracy and spatial resolution are insufficient, especially for discontinuous or spatially isolated surface topography [167]. Difficulties in measuring surface shape with sharp boundaries are attributed not only to the interference of the perceptible reflected lights outside the NA but also to inadequate grid size to resolve steep height difference [197]. Continuous information during the discrete scan steps can be obtained when a large tilt for the tested object with large discontinuities is used to ensure visible fringes at each scan step. The gap in fringe information between different scanner positions can be reduced by extending the spatial or temporal coherence of the light source [198].

High surface slopes may result in low fringe contrast. More data points containing larger systematic errors will be introduced under a lower modulation threshold. Furthermore, low fringe contrast or high surface slopes can cause a CSI instrument to be prone to data dropout [199]. The NA of the objective is a key determining factor in surface slope angle tolerance. The high-NA objective is preferred to overcome the slope limits for optical interferometry, even if the high magnification is not needed in practice. A high-sloped surface that is beyond the reach of the high-NA objective usually requires an enhanced sensitivity of the instrument [32]. Dynamic noise reduction (DNR) for detecting weak signals allows a trade-off between the throughput and sensitivity, boosting dynamic measurement range without sacrificing

performance [200]. As shown in Fig. 10, data coverage is nearly complete for both a polymer microlens with slopes up to 60° and a retroreflector array with slopes beyond the specular limit. However, the increase in measurement time is a critical issue. A software tool that processes images through controlled tilt is also useful to increase the maximum detectable slope of optical interferometers [201].

5.1.3 Vibration sensitivity

Another clear challenge facing the interference microscope is vibration sensitivity. Unexpected vibrations can significantly degrade measurement accuracy [202]. Currently, a commercial optical interferometer is usually configured as a benchtop platform of interference microscopy equipped with multi-axis motion stages, turreted objectives, and an integrated vibration isolation system. This instrument can perform highly repeatable measurements in a well-controlled environment, but it cannot be applicable to manufacturing sites for on-line or on-machine measurement due to the vibration vulnerability and noise.

Even nanoscale vibrations can cause the measurement system to incorrectly record the phase value or envelope peak position [203]. Unexpected vibrations often incorporate multiple components, such as vibration of the base, machine-induced vibration, and vibration of the PZT scanner, which have multi-scale and multi-dimensional characteristics. Compensation for machine-induced vibration is a challenging task due to its random nature and wide bandwidth that can induce non-repeatable error components [30]. Accordingly, the kinematic and dynamic properties of the machine need to be fully investigated. Furthermore, compensating for PZT scanning error is difficult because its frequency and amplitude are much closer to the actual surface height. In addition to further

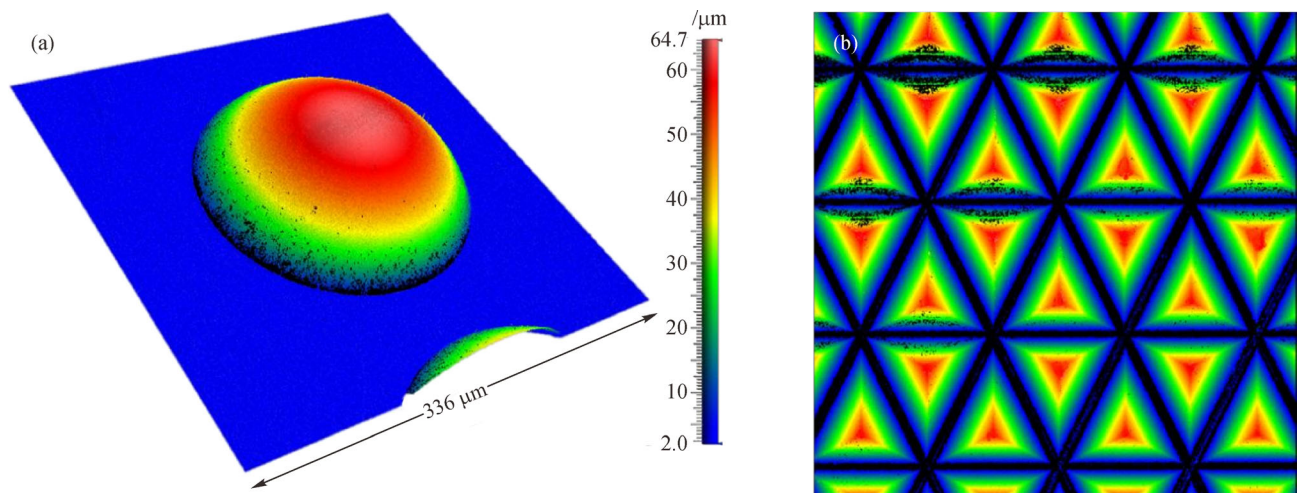


Fig. 10 Measurements of (a) polymer microlens using 3X DNR and (b) retroreflector array using 4X DNR [200]. DNR: Dynamic noise reduction. Courtesy of Martin Fay (ZYGO).

optimizing the control strategy for the PZT scanner and scanning rate, fringe analysis algorithms are expected to offer more powerful anti-noise ability and filtering ability. Specified frequency components corresponding to the vibration of the PZT scanner should be identified and eliminated precisely from the measurement results without losing any significant surface information.

The resistance of PSI to vibration can be enhanced by accelerating the data collection and suppressing the scanning error [204]. High-speed image data acquisition can lessen the effect of low-frequency drifts, and phase correction algorithm based on HT can correct distorted interferograms with regard to higher frequency vibrations [205]. In addition, AIA is an effective way to desensitize the vibration effect. In iterative calculation, all variables are treated as unknowns and the wavefront phase is achieved by iteratively solving algebraic equations [206].

5.1.4 Lateral resolution

A generally recognized drawback of optical interferometry is its lateral resolution. The lateral resolution of an interferometric instrument completely falls behind its vertical resolution [207,208]. The lateral resolution also plays an important role in surface topography reconstruction, particularly in the measurement of ultra-fine structures. The NA of an objective lens significantly contributes to the lateral resolution. The selection of an applicable lens needs to balance multiple competing variables, such as resolution, field of view (FOV), and working distance [32]. If a higher lateral resolution is desired, then a smaller working distance and FOV are needed. In this case, aside from the reduced area of interest on the target surface, the operation may be inconvenient for the measurement of some complex components such as conical or concave surfaces.

This issue discussed above imposes many challenges on the measurement of complex micro/nanostructured surfaces. In addition to the powerful fringe analysis algorithms, digital holographic interferometry (DHI) offers the possibility of extending the resolution beyond the Rayleigh limit of the objective [209]. The special information carried by the phase in DHI can be utilized to measure objects with surface discontinuities, such as holes, steps, and gaps [210]. As a promising approach, DHI has been widely employed in the measurement and characterization of MEMS [13,14], microlens arrays [211], and biological specimens [15,16].

5.2 Perspective

5.2.1 Global surface topography measurement

Reasonable performance characterization of an ultra-precision complex surface generally requires a global

surface topography measurement and evaluation. The available measurement areas are determined by the objective magnification, zoom lens, and camera [32]. The typical measurement area of a CSI instrument ranges from several tens of microns to several hundred microns due to this limitation. When the FOV of a lens is smaller than the surface area to be tested, the stitching function allows the realization of a global surface map whereby a group of images captured at different positions are stitched together [212]. The stitching algorithm is essential for processing overlapped images to correctly correlate the lateral position and consistent vertical height [199]. The available measurement area can be significantly extended not only for flat surfaces [213] but also for spherical and aspherical surfaces [214,215].

Notably, the stitching procedures will inevitably introduce multiple errors, including positioning errors of the motion stages, viewing distortion, and reference wave error of the interference system [216]. During the construction of a full-aperture phase map, the stitching errors will increase rapidly with the increase in the number of sub-apertures [17]. A height quality matrix can be obtained to distinguish the noises from effective heights in 3D images to improve the stitching accuracy. As shown in Fig. 11, the neighbor effective heights along four directions are used to reconstruct the height-unknown regions and eliminate the noise in 3D image stitching [217]. In addition, new objectives with wide FOV, good compatibility, and compact structure are expected to further promote the global surface topography measurement.

5.2.2 On-machine measurement

Complex-shaped components with nanometric accuracy such as freeform optics are increasingly needed in diverse areas. On-machine measurement offers great promise for manufacturing such components that have geometric complexity and high accuracy, avoiding the non-working time and reclamping efforts. Accordingly, the coordinate system of the machining and measuring process is consistent inside the machine tool. The error compensation methods based on on-machine measurement results are believed to be effective ways to correct the machining errors [218]. Currently, two main strategies are used for error compensation: Real-time compensation by computer numerical control (CNC) system [219,220] and pre-compensation by adjusting the tool path for the designed model [221,222]. Figure 12 shows the compensation strategy for machining freeform surfaces by the combined on- and off-machine measurements.

A variety of on-machine measurement systems (e.g., linear variable differential transformer (LVDT) [8], optical slope sensor [223], AFM head [224], force sensor-integrated fast tool servo [225], and chromatic confocal probe [226]) have been developed for form error

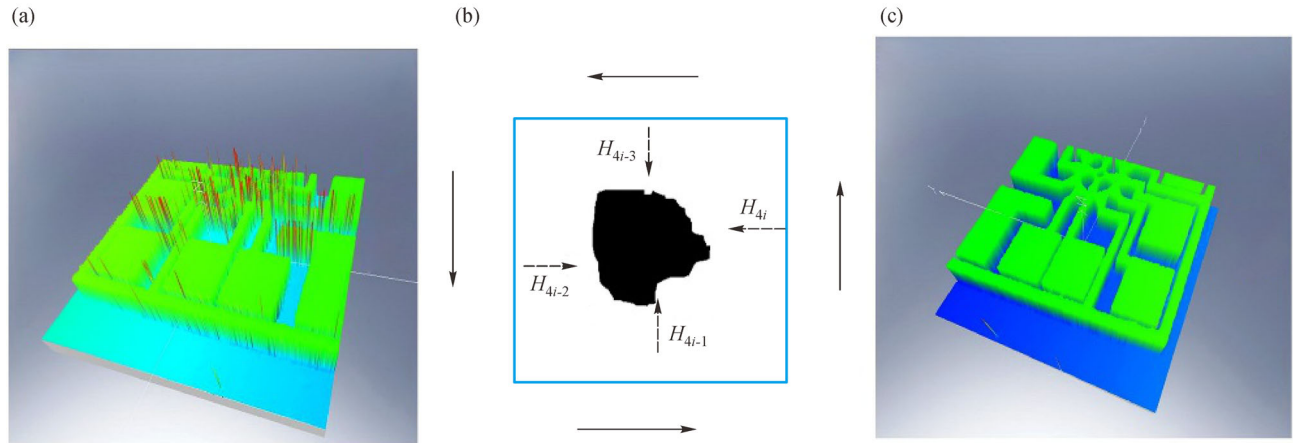


Fig. 11 Principle for reconstruction algorithm: (a) Original 3D image, (b) reconstruction approach for a height-unknown region (black region) in the 3D image by the neighbor effective height region (white region), and (c) 3D image achieved after reconstruction. Reproduced from Ref. [217] with permission from Elsevier.

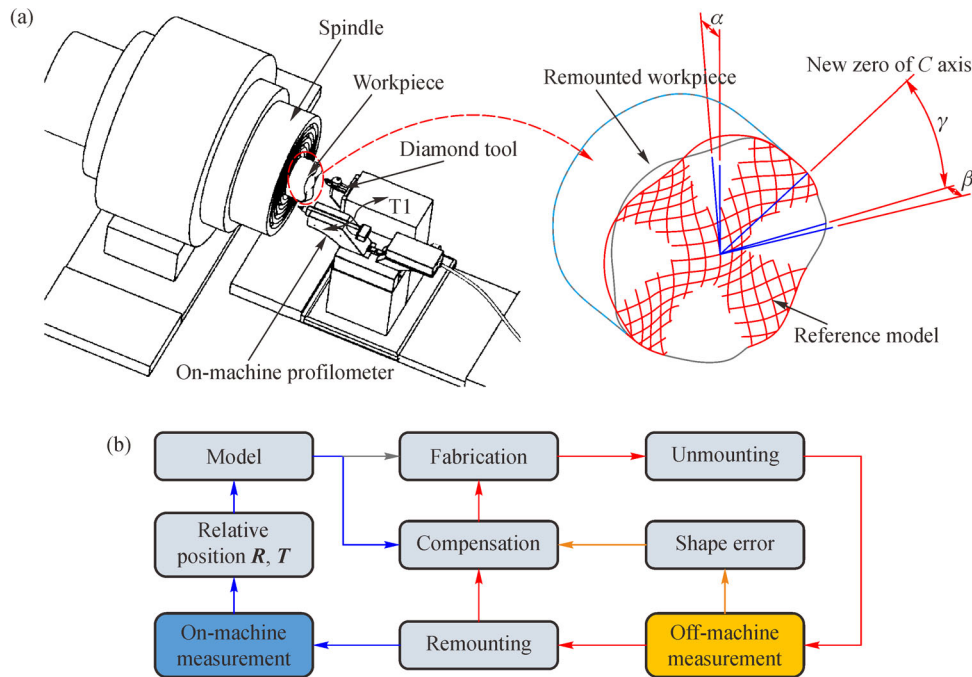


Fig. 12 Compensation strategy for machining an optical freeform surface: (a) Schematic of on-machine profilometer and (b) process flow. Adapted with permission from Ref. [7]. © The Optical Society.

compensation of complex surfaces, avoiding a repositioning error and extending the measuring range through the machine axis motions. Optical interferometry is a great choice for non-contact on-machine surface measurement [26,227], providing high resolution, high accuracy, and low uncertainty. As a nondestructive tool, optical interferometer outperforms LVDT when measuring microstructured surfaces and ultra-precision machined surfaces. A Twyman–Green phase-shifting interferometer has been employed to conduct on-machine form measurement of

mid-infrared instrument mirrors [27]. A surface map of V-grooves can be reconstructed by an on-machine WSI system and image stitching method in a diamond turning machine (DTM) [28].

To reduce uncertainty, maximum attention needs to be paid to machine axis misalignments with the interferometric sensor [201]. Ideally, the axis of the interference microscope is commonly kept normal to the local surface slope to achieve high accuracy. Therefore, for on-machine measurement, the interferometric sensors need to be

accurately positioned and calibrated in the coordinate system of the machine tool. As shown in Fig. 13, an interferometric on-machine probing system is integrated into a three-axis DTM. A machine scanning error model has been established to calibrate this on-machine measurement system [228,229]. Even though on-machine measurement and compensation still face many difficulties in practical applications (e.g., the disturbance of cutting fluid and chips, the vibration of the machine tool, the accessibility of CNC controller, and the data acquisition speed), it is undoubtedly evolving as the key enabling technology to improve machining accuracy and surface quality, boosting the machining-metrology integration. During this trend, the features of miniaturization, noise resistance, and ultra-high-speed data acquisition will become increasingly important.

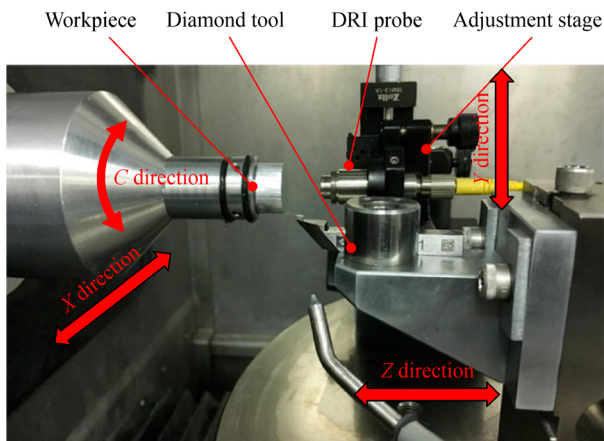


Fig. 13 On-machine measurement system based on dispersed reference interferometry. DRI: Dispersed reference interferometry. Reproduced from Ref. [228] with permission from Elsevier.

5.2.3 Intelligent sampling strategy

Using the fewest measurements to obtain the most reliable results has always been the most desirable strategy. Optical interferometric measurement requires accurate phase shifts or scanning motions to acquire fringe images and relatively complicated computation to recover surface profile. The time-consuming measurement process is also considered a process of error accumulation, which is inevitably affected by mechanical vibration and air turbulence. Hence, a reasonable sampling strategy with low measurement uncertainty and high measurement efficiency is important. Sub-aperture stitching can give a form error map for the global surface. However, this technique is inherently more complicated for complex surfaces such as freeform surfaces. The sampling strategy for a freeform surface is typically dependent on its curvature, generally requiring a higher point density for a high curvature region [6]. The curvature change-based sampling algorithm adopts the variation of surface curvature to identify the optimal sampling location [230].

The adaptive sampling strategy determines the locations of the sampling points based on various features of the inspected surfaces, providing more accurate measurement results than blind strategies [231]. As shown in Fig. 14, wavelet decomposition is employed to extract the key points set that represents the scanning data [232]. To shorten the production cycle, spatio-temporal adaptive sampling is proposed to inspect freeform components [233,234]. Intelligent adaptive sampling methods based on the Gaussian process have been demonstrated to efficiently reconstruct structured, freeform, and multi-scale surface geometries [235,236]. Figure 15 shows the framework of a multi-sensor data fusion algorithm for intelligent sampling [237]. An intelligent sampling strategy has the potential to improve both the efficiency and accuracy of high-density

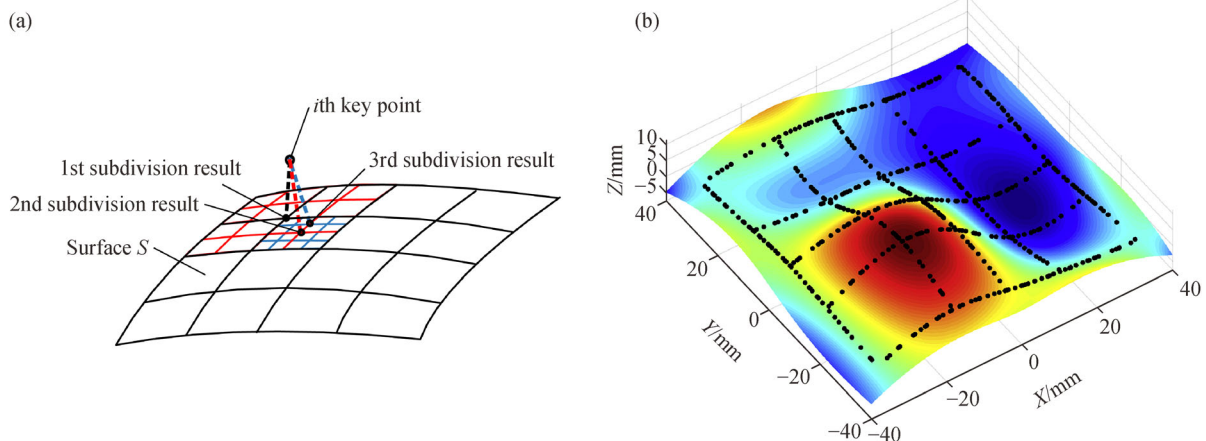


Fig. 14 Profile error evaluation method for freeform surface: (a) Surface subdivision method and (b) key points distribution extracted from the scanning lines. Reproduced from Ref. [232] with permission from Elsevier.

measurements, enhancing the surface reconstruction algorithm for interferometric measurement. More applications of intelligent sampling are expected in the measurement of large-area freeform and structured surfaces.

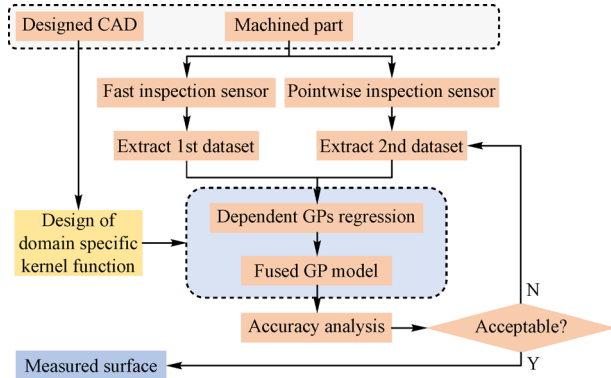


Fig. 15 Framework of the intelligent sampling strategy. GP: Gaussian process. Reproduced from Ref. [237] with permission from Elsevier.

5.2.4 Parallel computing

Many efforts have been put into the pursuit of high accuracy in optical interferometric measurements. Higher measurement resolution and accuracy always mean more demanding data acquisition and processing efficiency. Meanwhile, more complicated algorithms would lead to additional computational expense. High-speed fringe analysis is also a desirable goal because real-time measurement shows immense research potential and is required in many areas. In addition to the smart realization of an algorithm, parallel computing is also a promising approach to accelerate the computation performance of optical interferometric measurements while providing the required accuracy [238,239]. The dramatic speedup

performance of a parallel WFT algorithm based on GPUs has been demonstrated in processing digital holographic fringe patterns [174]. Moreover, real-time 3D shape measurement can be realized through parallel strategies [240,241]. Hence, the advantages of parallel hardware platforms and algorithms for boosting computation performance are remarkable. One can consider employing the parallel computing method to conduct on-machine or even in-process measurement of a large complex work-piece such as a roller mold. In future surface metrology, parallel computing will provide more possibilities to achieve the desired accuracy, robustness, speed, and flexibility simultaneously in various areas.

5.2.5 Deep learning

As a powerful machine learning technique, deep learning employs a multi-layered artificial neural network and has found considerable applications in imaging science [242]. A deep neural network can significantly improve the performance of optical microscopy, enhancing its spatial resolution, FOV, and depth of field [243]. The deep learning-based technique has been used to perform phase recovery and holographic image reconstruction using only one hologram intensity [244]. Feng et al. [167] employed a deep neural network to improve the accuracy of phase demodulation from an input fringe pattern. Compared with FT and WFT methods, the deep learning-based method is more accurate and can effectively perform temporal phase unwrapping even under harsh conditions [245]. A properly trained deep neural network is capable of high-quality 3D shape reconstructions for transient scenes [246]. As shown in Fig. 16, several intermediate results obtained through network training are used to retrieve a high-accuracy phase map.

Deep learning techniques provide promising potential for fringe analysis, even though the computation burden of training the fringe pattern set becomes much heavier.

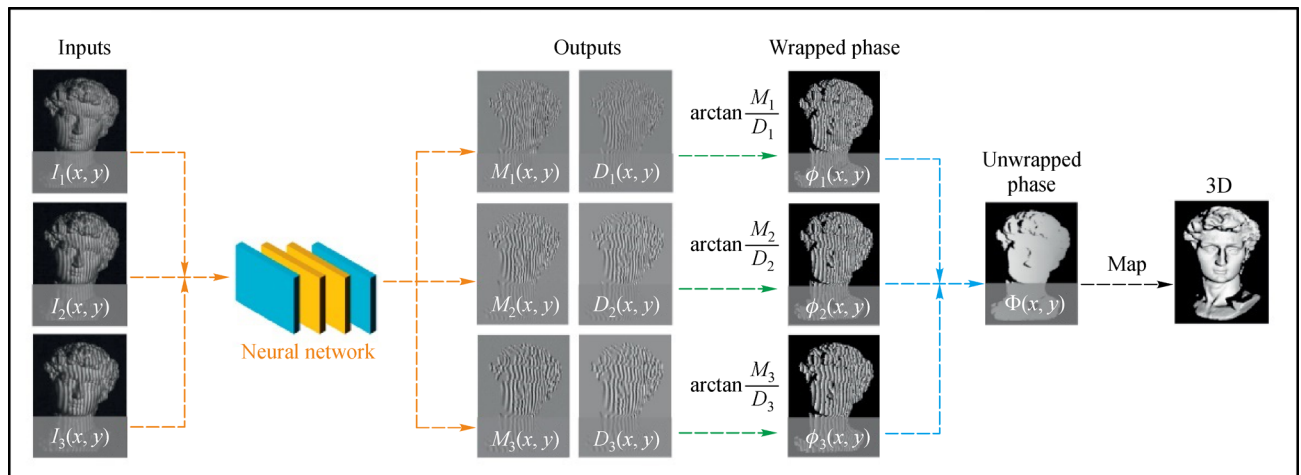


Fig. 16 Schematic of micro deep learning profilometry. Reproduced from Ref. [246] with permission from Elsevier.

Notably, the estimation accuracy of a deep learning-based algorithm greatly depends on how well the network training is performed. The selection of appropriate fringe patterns to be trained is an important step. Fringe patterns with sufficient frequency and SNR, adequate density, and contrast are preferred. The best network model for a specific object can be determined by the trained images and optimized parameters, thereby significantly reducing the data usage and complexity of the network. Therefore, surface reconstruction algorithms based on deep learning will find immensely promising applications in optical interferometric profilometry. The integration of DHI and parallel computing techniques with deep learning will certainly be an attractive area of surface metrology.

6 Conclusions

The functional performance of a machined workpiece can be traced to its surface topography. The past decades have witnessed the tremendous development of 3D surface metrology in various applications. Optical interferometric techniques are proven to yield reliably generalizable solutions to metrological characteristic tasks. To provide a comprehensive insight into the measurement of engineered surfaces in precision manufacturing, this paper summarizes typical optical interferometry techniques and surface reconstruction methods. An attempt is made to review the existing fringe analysis algorithms, which are mainly divided into the categories of CPS and PSA. The selection of an appropriate algorithm is always a trade-off between accuracy, robustness, resolution, and computational efficiency.

Topographical surface analysis based on optical interferometry has continuously evolved. Currently, accessible surface geometry for optical interferometry ranges from simple flat and stepped surfaces to complex surfaces such as sphere/asphere, transparent film, freeform surface, and micro/nanostructured surface. Improved fringe analysis algorithms have promising potential to process very weak interference signals by using emerging technologies and tools, also providing high accuracy and speed. Algorithms with strong noise resistance and self-calibration ability have also enjoyed notable development because they are capable of reliable fringe analysis and topography reconstruction under harsh conditions. Moreover, the algorithms that combine the benefits of the phase-shift method and coherence envelope detection provide more possibilities to perform intricate measurement tasks.

A desirable but also challenging task for fringe analysis algorithms is to be as accurate as possible with the fewest fringe patterns. Some challenges and drawbacks still need to be overcome, such as miscalibration error, vibration sensitivity, and lateral resolution. Surface discontinuities and high slopes may degrade the fringe contrast. A

controlled tilt for the tested object can alleviate this limitation. Global surface topography measurement is a promising research trend, in which the image stitching technique and intelligent sampling strategy will be more crucial in expanding the measurable area and sample size. On-machine measurement is expected to be an essential part of future precision/ultra-precision manufacturing, avoiding repositioning error and allowing immediate measurement after the manufacturing process. Furthermore, parallel computing and deep learning will play an increasingly important role in the fast and accurate reconstruction of complex surface topography. The research progress discussed above will contribute to the deep integration of future manufacturing and metrology.

Nomenclature

Abbreviations

A	Analyzer
AFM	Atomic force microscope
AIA	Advanced iterative algorithm
AOM	Acousto-optical modulator
AOTF	Acousto-optic tunable filter
ASSF	Advanced spatial spectrum fitting
BS	Beam splitter
CCD	Charge coupled device
CGH	Computer generated hologram
CLSM	Confocal laser scanning microscopy
CNC	Computer numerical control
CPS	Coherence peak sensing
CSI	Coherence scanning interferometry
CWT	Continuous wavelet transform
DAQ	Data acquisition card
DHI	Digital holographic interferometry
DNR	Dynamic noise reduction
DRI	Dispersed reference interferometry
DTM	Diamond turning machine
FDA	Frequency domain analysis
FFT	Fast Fourier transform
FOV	Field of view
FT	Fourier transform
GP	Gaussian process
GPU	Graphics processing unit
HHT	Hilbert–Huang transform
HI	Heterodyne interferometry
HT	Hilbert transform
IMAQ	Image acquisition board
IR SLED	Near-infrared superluminescent light-emitting diode

L1	Collimating lens	$\psi_{a,b}(z)$	A complete set of daughter wavelets
L2, L3	Microscope objectives	ϕ	Interferometric phase
LED	Light emitting diode	$\phi(z)$	Wavefront phase
LVDT	Linear variable differential transformer	a	Scaling factor of CWT
MEMS	Micro-electromechanical systems	b	Shift factor of CWT
MO	Microscope objectives	$A(x, y)$	Amplitudes of the signals reflected from the sample
MSSM	Mid-band spatial spectrum matching	B	Amplitudes of the signals reflected from the reference mirror
NA	Numerical aperture	f	NA factor of the interference objective
OPD	Optical path difference	f_b	Bandwidth of the mother wavelet
P	Polarizer	f_c	Center frequency
PC	Personal computer	$f(z)$	Modulation function
PCA	Principal component analysis	G	Group velocity OPD
PD	Photodiode	$h_{\text{norm}}(n)$	Normalized impulse response
PSA	Phase-shifting algorithm	$H(e^{j\omega})$	Frequency response
PSI	Phase-shifting interferometry	$i_{xy}(n)$	Unbiased image
PV	Peak-to-valley	$i_{xy} * (n)$	$\pi/2$ phased-shifted image from $i_{xy}(n)$
PZT	Piezoelectric transducer	$I(x, y, z)$	Output signal from the CCD camera
QW1, QW2	Quarter wave plates	I_{AB}	Correlation term
REF	Reference mirror	I_{AB}^d	Demodulated correlation term
RMS	Root mean square	I_0	Constant background intensity
SD-OCT	Spectral domain optical coherence tomography	$I_{xy}(n)$	Input image
S2H2PM	Single-shot Hilbert–Huang phase microscopy	$I(z)$	Interferogram
SNR	Signal-to-noise ratio	$I_i(z) (i = 1, 2, \dots, 7)$	Consecutive fringe intensities
SWLI	Scanning white-light interferometry	$I(Z_i)$	Interference function
TKEO	Teager–Kaiser energy operator	j	Imaginary unit
USFP	Ultra-sparse fringe pattern	k	Angular wavenumber of the light source
VSI	Vertical scanning interferometry	k_0	Mean wavenumber
WFF	Windowed Fourier filtering	k_z	Spatial frequency
WFR	Windowed Fourier ridges	l	Fringe order
WFT	Windowed Fourier transform	$M(z)$	Fringe visibility (also called modulation)
WLI	White light interferometry	N	Step number
WLPSI	White-light phase-shifting interferometry	$P(k_j)$	For a particular wavenumber k_j , the j th component of the FT
WLSI	White-light scanning interferometry	Rq	Root mean square deviation
WS-DHM	Wavelength scanning digital holographic microscope	$Sf(u, \xi)$	WFT spectrum
WSI	Wavelength scanning interferometry	u	Translated coordinate
WT	Wavelet transform	$V_{xy}(n)$	Demodulation function
ZOPD	Zero optical path difference	$w(x)$	Window function
Symbols		$W_I(a, b)$	Correlation coefficient of one-dimensional CWT
		(x, y)	Spatial coordinates
λ	Wavelength	z	Scanning position
$\bar{\lambda}$	Mean wavelength	$z_0(x, y)$	Surface profile height
$\gamma(x, y, z)$	Cross correlation	Δz	Step size
$\varphi[(z - z_0(x, y))]$	Phase variation	Z	OPD
ξ	Frequency center	Z_i	Equally-spaced OPD positions
ω	Angular frequency	*	Complex conjugate

Acknowledgements This work received funding from the Enterprise Ireland and from the European Union's Horizon 2020 Research and Innovation Programme under the Marie Skłodowska-Curie grant agreement (Grant No. 713654), the National Natural Science Foundation of China (Grant No. 51705070), and the Science Foundation Ireland (SFI) (Grant No. 15/RP/B3208). The authors appreciate the fruitful discussions and suggestions from Szymon Baron of DePuy Synthes. The authors would also like to thank Chengwei Kang of University College Dublin for his comments on the paper.

Open Access This article is licensed under a Creative Commons Attribution 4.0 International License, which permits use, sharing, adaptation, distribution and reproduction in any medium or format, as long as you give appropriate credit to the original author(s) and the source, provide a link to the Creative Commons licence, and indicate if changes were made.

The images or other third-party material in this article are included in the article's Creative Commons licence, unless indicated otherwise in a credit line to the material. If material is not included in the article's Creative Commons licence and your intended use is not permitted by statutory regulation or exceeds the permitted use, you will need to obtain permission directly from the copyright holder.

To view a copy of this licence, visit <http://creativecommons.org/licenses/by/4.0/>.

References

- Brinksmeier E, Gläbe R, Schönemann L. Review on diamond-machining processes for the generation of functional surface structures. *CIRP Journal of Manufacturing Science and Technology*, 2012, 5(1): 1–7
- Jain V, Ranjan P, Suri V, et al. Chemo-mechanical magnetorheological finishing (CMMRF) of silicon for microelectronics applications. *CIRP Annals-Manufacturing Technology*, 2010, 59(1): 323–328
- Yamamura K, Takiguchi T, Ueda M, et al. Plasma assisted polishing of single crystal SiC for obtaining atomically flat strain-free surface. *CIRP Annals-Manufacturing Technology*, 2011, 60(1): 571–574
- Schmidt M, Merklein M, Bourell D, et al. Laser based additive manufacturing in industry and academia. *CIRP Annals-Manufacturing Technology*, 2017, 66(2): 561–583
- Hocken R, Chakraborty N, Brown C. Optical metrology of surfaces. *CIRP Annals-Manufacturing Technology*, 2005, 54(2): 169–183
- Savio E, De Chiffre L, Schmitt R. Metrology of freeform shaped parts. *CIRP Annals-Manufacturing Technology*, 2007, 56(2): 810–835
- Zhang X D, Zeng Z, Liu X L, et al. Compensation strategy for machining optical freeform surfaces by the combined on- and off-machine measurement. *Optics Express*, 2015, 23(19): 24800–24810
- Liu X L, Zhang X D, Fang F Z, et al. Identification and compensation of main machining errors on surface form accuracy in ultra-precision diamond turning. *International Journal of Machine Tools and Manufacture*, 2016, 105: 45–57
- Shore P, Cunningham C, DeBra D, et al. Precision engineering for astronomy and gravity science. *CIRP Annals-Manufacturing Technology*, 2010, 59(2): 694–716
- Takaya Y. In-process and on-machine measurement of machining accuracy for process and product quality management: A review. *International Journal of Automotive Technology*, 2014, 8(1): 4–19
- Lee J C, Shimizu Y, Gao W, et al. Precision evaluation of surface form error of a large-scale roll workpiece on a drum roll lathe. *Precision Engineering*, 2014, 38(4): 839–848
- Novak E, Stout T. Interference microscopes for tribology and corrosion quantification. In: *Proceedings of SPIE 6616, Optical Measurement Systems for Industrial Inspection V*. Munich: SPIE, 2007, 66163B
- Coppola G, Ferraro P, Iodice M, et al. A digital holographic microscope for complete characterization of microelectromechanical systems. *Measurement Science and Technology*, 2004, 15(3): 529–539
- Singh V R, Asundi A. In-line digital holography for dynamic metrology of MEMS. *Chinese Optics Letters*, 2009, 7(12): 1117–1122
- Potcoava M, Kim M. Optical tomography for biomedical applications by digital interference holography. *Measurement Science and Technology*, 2008, 19(7): 074010
- Merola F, Memmolo P, Miccio L, et al. Tomographic flow cytometry by digital holography. *Light, Science & Applications*, 2017, 6(4): e16241
- Fang F Z, Zhang X D, Weckenmann A, et al. Manufacturing and measurement of freeform optics. *CIRP Annals-Manufacturing Technology*, 2013, 62(2): 823–846
- Taylor Hobson Ltd. Form Talysurf PGI Optics Surface Profilometers Brochure. Available from Taylor Hobson website, 2018
- Bruker Corporation. Dimension Icon Atomic Force Microscope Brochure. Available from Bruker website, 2013
- Zygo Corporation. NewView™ 9000 3D Optical Surface Profiler Brochure. Available from Zygo website, 2018
- OLYMPUS Corporation. LEXT OLS5000 3D Measuring Laser Microscope Brochure. Available from OLYMPUS website, 2018
- Moore Nanotech. Workpiece measurement and Error Compensation System (WECS) Brochure. Available from Moore Nanotech website, 2020
- Vorburger T V, Rhee H G, Renegar T B, et al. Comparison of optical and stylus methods for measurement of surface texture. *International Journal of Advanced Manufacturing Technology*, 2007, 33(1–2): 110–118
- Villarrubia J S. Algorithms for scanned probe microscope image simulation, surface reconstruction, and tip estimation. *Journal of Research of the National Institute of Standards and Technology*, 1997, 102(4): 425
- Wang Y, Xie F, Ma S, et al. Review of surface profile measurement techniques based on optical interferometry. *Optics and Lasers in Engineering*, 2017, 93: 164–170
- Nomura T, Yoshikawa K, Tashiro H, et al. On-machine shape measurement of workpiece surface with Fizeau interferometer. *Precision Engineering*, 1992, 14(3): 155–159
- Shore P, Morantz P, Lee D, et al. Manufacturing and measurement of the MIRI spectrometer optics for the James Webb space telescope. *CIRP Annals-Manufacturing Technology*, 2006, 55(1): 543–546
- Jiang X. *In situ* real-time measurement for micro-structured surfaces. *CIRP Annals-Manufacturing Technology*, 2011, 60(1): 563–566

29. Wang D, Fu X, Xu P, et al. Compact snapshot dual-mode interferometric system for on-machine measurement. *Optics and Lasers in Engineering*, 2020, 132: 106129
30. Gao W, Haitjema H, Fang F Z, et al. On-machine and in-process surface metrology for precision manufacturing. *CIRP Annals-Manufacturing Technology*, 2019, 68(2): 843–866
31. Li D, Wang B, Tong Z, et al. On-machine surface measurement and applications for ultra-precision machining: A state-of-the-art review. *International Journal of Advanced Manufacturing Technology*, 2019, 104(1–4): 831–847
32. de Groot P. Principles of interference microscopy for the measurement of surface topography. *Advances in Optics and Photonics*, 2015, 7(1): 1–65
33. Zuo C, Feng S, Huang L, et al. Phase shifting algorithms for fringe projection profilometry: A review. *Optics and Lasers in Engineering*, 2018, 109: 23–59
34. Malacara D. *Optical Shop Testing*. Hoboken: John Wiley & Sons, 2007, 547–666
35. Creath K. V phase-measurement interferometry techniques. *Progress in Optics*, 1988, 26: 349–393
36. Cheng Y Y, Wyant J C. Multiple-wavelength phase-shifting interferometry. *Applied Optics*, 1985, 24(6): 804–807
37. Lannes A. Integer ambiguity resolution in phase closure imaging. *Journal of the Optical Society of America. A, Optics, Image Science, and Vision*, 2001, 18(5): 1046–1055
38. Fornaro G, Franceschetti G, Lanari R, et al. Robust phase-unwrapping techniques: A comparison. *Journal of the Optical Society of America. A, Optics, Image Science, and Vision*, 1996, 13(12): 2355–2366
39. Davé D P, Akkin T, Milner T E, et al. Phase-sensitive frequency-multiplexed optical low-coherence reflectometry. *Optics Communications*, 2001, 193(1–6): 39–43
40. Wyant J C. White light interferometry. *Proceedings of SPIE 4737, Holography: A Tribute to Yuri Denisjuk and Emmett Leith*, 2002, 98–108
41. Cheng Y Y, Wyant J C. Two-wavelength phase shifting interferometry. *Applied Optics*, 1984, 23(24): 4539–4543
42. Onodera R, Ishii Y. Two-wavelength phase-shifting interferometry insensitive to the intensity modulation of dual laser diodes. *Applied Optics*, 1994, 33(22): 5052–5061
43. Abdelsalam D, Kim D. Two-wavelength in-line phase-shifting interferometry based on polarizing separation for accurate surface profiling. *Applied Optics*, 2011, 50(33): 6153–6161
44. Decker J E, Miles J R, Madej A A, et al. Increasing the range of unambiguity in step-height measurement with multiple-wavelength interferometry—Application to absolute long gauge block measurement. *Applied Optics*, 2003, 42(28): 5670–5678
45. Warnasooriya N, Kim M. LED-based multi-wavelength phase imaging interference microscopy. *Optics Express*, 2007, 15(15): 9239–9247
46. Schmit J, Hariharan P. Two-wavelength interferometric profilometry with a phase-step error-compensating algorithm. *Optical Engineering*, 2006, 45(11): 115602
47. Pfortner A, Schwider J. Red-green-blue interferometer for the metrology of discontinuous structures. *Applied Optics*, 2003, 42(4): 667–673
48. Upputuri P K, Mohan N K, Kothiyal M P. Measurement of discontinuous surfaces using multiple-wavelength interferometry. *Optical Engineering*, 2009, 48(7): 073603
49. Caber P J. Interferometric profiler for rough surfaces. *Applied Optics*, 1993, 32(19): 3438–3441
50. Sandoz P, Devillers R, Plata A. Unambiguous profilometry by fringe-order identification in white-light phase-shifting interferometry. *Journal of Modern Optics*, 1997, 44(3): 519–534
51. Debnath S K, Kothiyal M P. Experimental study of the phase-shift miscalibration error in phase-shifting interferometry: Use of a spectrally resolved white-light interferometer. *Applied Optics*, 2007, 46(22): 5103–5109
52. Yang C, Wax A, Dasari R R, et al. 2π ambiguity-free optical distance measurement with subnanometer precision with a novel phase-crossing low-coherence interferometer. *Optics Letters*, 2002, 27(2): 77–79
53. Deck L, de Groot P. High-speed noncontact profiler based on scanning white-light interferometry. *Applied Optics*, 1994, 33(31): 7334–7338
54. Harasaki A, Schmit J, Wyant J C. Improved vertical-scanning interferometry. *Applied Optics*, 2000, 39(13): 2107–2115
55. Balasubramanian N. US Patent, 4340306, 1982-07-20
56. Kumar U P, Haifeng W, Mohan N K, et al. White light interferometry for surface profiling with a colour CCD. *Optics and Lasers in Engineering*, 2012, 50(8): 1084–1088
57. Gianto G, Salzenstein F, Montgomery P. Comparison of envelope detection techniques in coherence scanning interferometry. *Applied Optics*, 2016, 55(24): 6763–6774
58. Gianto G, Montgomery P, Salzenstein F, et al. Study of robustness of 2D fringe processing in coherence scanning interferometry for the characterization of a transparent polymer film. In: *Proceedings of 2016 International Conference on Instrumentation, Control and Automation (ICA)*. Bandung: IEEE, 2016, 60–65
59. Zhou Y, Cai H, Zhong L, et al. Eliminating the influence of source spectrum of white light scanning interferometry through time-delay estimation algorithm. *Optics Communications*, 2017, 391: 1–8
60. de Groot P. Coherence scanning interferometry. In: Leach R, ed. *Optical Measurement of Surface Topography*. Berlin: Springer, 2011, 187–208
61. Fang F Z, Zeng Z, Zhang X D, et al. Measurement of micro-V-groove dihedral using white light interferometry. *Optics Communications*, 2016, 359: 297–303
62. de Groot P, Deck L. Surface profiling by analysis of white-light interferograms in the spatial frequency domain. *Journal of Modern Optics*, 1995, 42(2): 389–401
63. Kino G S, Chim S S. Mirau correlation microscope. *Applied Optics*, 1990, 29(26): 3775–3783
64. Bowe B W, Toal V. White light interferometric surface profiler. *Optical Engineering*, 1998, 37(6): 1796–1800
65. Lehmann P, Tereschenko S, Xie W. Fundamental aspects of resolution and precision in vertical scanning white-light interferometry. *Surface Topography: Metrology and Properties*, 2016, 4(2): 024004
66. Yamaguchi I, Yamamoto A, Yano M. Surface topography by wavelength scanning interferometry. *Optical Engineering*, 2000,

- 39(1): 40–47
67. Yamamoto A, Yamaguchi I. Profilometry of sloped plane surfaces by wavelength scanning interferometry. *Optical Review*, 2002, 9(3): 112–121
68. Kuwamura S, Yamaguchi I. Wavelength scanning profilometry for real-time surface shape measurement. *Applied Optics*, 1997, 36(19): 4473–4482
69. Yamamoto A, Kuo C C, Sunouchi K, et al. Surface shape measurement by wavelength scanning interferometry using an electronically tuned Ti: Sapphire laser. *Optical Review*, 2001, 8(1): 59–63
70. Yamamoto A, Yamaguchi I. Surface profilometry by wavelength scanning Fizeau interferometer. *Optics & Laser Technology*, 2000, 32(4): 261–266
71. Ishii Y. Wavelength-tunable laser-diode interferometer. *Optical Review*, 1999, 6(4): 273–283
72. Jiang X, Wang K, Gao F, et al. Fast surface measurement using wavelength scanning interferometry with compensation of environmental noise. *Applied Optics*, 2010, 49(15): 2903–2909
73. Muhamedsalih H, Jiang X, Gao F. Comparison of fast Fourier transform and convolution in wavelength scanning interferometry. *Proceedings of SPIE 8082, Optical Measurement Systems for Industrial Inspection VII*, 2011, 8082: 80820Q
74. Gao F, Muhamedsalih H, Jiang X. Surface and thickness measurement of a transparent film using wavelength scanning interferometry. *Optics Express*, 2012, 20(19): 21450–21456
75. Muhamedsalih H, Jiang X, Gao F. Accelerated surface measurement using wavelength scanning interferometer with compensation of environmental noise. *Procedia CIRP*, 2013, 10: 70–76
76. Moschetti G, Forbes A, Leach R K, et al. Phase and fringe order determination in wavelength scanning interferometry. *Optics Express*, 2016, 24(8): 8997–9012
77. Zhang T, Gao F, Jiang X. Surface topography acquisition method for double-sided near-right-angle structured surfaces based on dual-probe wavelength scanning interferometry. *Optics Express*, 2017, 25(20): 24148–24156
78. Zhang T, Gao F, Muhamedsalih H, et al. Improvement of the fringe analysis algorithm for wavelength scanning interferometry based on filter parameter optimization. *Applied Optics*, 2018, 57(9): 2227–2234
79. Swanson E A, Huang D, Hee M R, et al. High-speed optical coherence domain reflectometry. *Optics Letters*, 1992, 17(2): 151–153
80. Huang Y C, Chou C, Chou L Y, et al. Polarized optical heterodyne profilometer. *Japanese Journal of Applied Physics*, 1998, 37(Part 1, No. 1): 351–354
81. Zhao H, Liang R, Li D, et al. Practical common-path heterodyne surface profiling interferometer with automatic focusing. *Optics & Laser Technology*, 2001, 33(4): 259–265
82. Demarest F C. High-resolution, high-speed, low data age uncertainty, heterodyne displacement measuring interferometer electronics. *Measurement Science & Technology*, 1998, 9(7): 1024–1030
83. Xie Y, Wu Y. Zeeman laser interferometer errors for high-precision measurements. *Applied Optics*, 1992, 31(7): 881–884
84. Gelmini E, Minoni U, Docchio F. Tunable, double-wavelength heterodyne detection interferometer for absolute-distance measurements. *Optics Letters*, 1994, 19(3): 213–215
85. Park Y, Cho K. Heterodyne interferometer scheme using a double pass in an acousto-optic modulator. *Optics Letters*, 2011, 36(3): 331–333
86. Matsumoto H, Hirai A. A white-light interferometer using a lamp source and heterodyne detection with acousto-optic modulators. *Optics Communications*, 1999, 170(4–6): 217–220
87. Hirai A, Matsumoto H. High-sensitivity surface-profile measurements by heterodyne white-light interferometer. *Optical Engineering*, 2001, 40(3): 387–392
88. Dai X, Katuo S. High-accuracy absolute distance measurement by means of wavelength scanning heterodyne interferometry. *Measurement Science & Technology*, 1998, 9(7): 1031–1035
89. Xu X, Wang Y, Ji Y, et al. A novel dual-wavelength iterative method for generalized dual-wavelength phase-shifting interferometry with second-order harmonics. *Optics and Lasers in Engineering*, 2018, 106: 39–46
90. Deck L L. Fourier-transform phase-shifting interferometry. *Applied Optics*, 2003, 42(13): 2354–2365
91. Kafri O. Fundamental limit on accuracy in interferometry. *Optics Letters*, 1989, 14(13): 657–658
92. Zhai Z, Li Z, Zhang Y, et al. An accurate phase shift extraction algorithm for phase shifting interferometry. *Optics Communications*, 2018, 429: 144–151
93. Vo Q, Fang F Z, Zhang X D, et al. Surface recovery algorithm in white light interferometry based on combined white light phase shifting and fast Fourier transform algorithms. *Applied Optics*, 2017, 56(29): 8174–8185
94. Chou C, Shyu J, Huang Y, et al. Common-path optical heterodyne profilometer: A configuration. *Applied Optics*, 1998, 37(19): 4137–4142
95. Chang W Y, Chen K H, Chen D C, et al. Heterodyne moiré interferometry for measuring corneal surface profile. *Optics and Lasers in Engineering*, 2014, 54: 232–235
96. Ajithaprasad S, Gannavarpu R. Non-invasive precision metrology using diffraction phase microscopy and space-frequency method. *Optics and Lasers in Engineering*, 2018, 109: 17–22
97. Venkata Satya Vithin A, Ajithaprasad S, Rajshekhar G. Step phase reconstruction using an anisotropic total variation regularization method in a diffraction phase microscopy. *Applied Optics*, 2019, 58(26): 7189–7194
98. Rajshekhar G, Bhaduri B, Edwards C, et al. Nanoscale topography and spatial light modulator characterization using wide-field quantitative phase imaging. *Optics Express*, 2014, 22(3): 3432–3438
99. Larkin K G. Efficient nonlinear algorithm for envelope detection in white light interferometry. *Journal of the Optical Society of America. A, Optics, Image Science, and Vision*, 1996, 13(4): 832–843
100. Kim J H, Yoon S W, Lee J H, et al. New algorithm of white-light phase shifting interferometry pursuing higher repeatability by using numerical phase error correction schemes of pre-processor, main processor, and post-processor. *Optics and Lasers in Engineering*, 2008, 46(2): 140–148
101. Tien C L, Yu K C, Tsai T Y, et al. Measurement of surface

- roughness of thin films by a hybrid interference microscope with different phase algorithms. *Applied Optics*, 2014, 53(29): H213–H219
102. Lei Z, Liu X, Chen L, et al. A novel surface recovery algorithm in white light interferometry. *Measurement*, 2016, 80: 1–11
 103. Muhamedsalih H, Gao F, Jiang X. Comparison study of algorithms and accuracy in the wavelength scanning interferometry. *Applied Optics*, 2012, 51(36): 8854–8862
 104. Sandoz P. Wavelet transform as a processing tool in white-light interferometry. *Optics Letters*, 1997, 22(14): 1065–1067
 105. Recknagel R J, Notni G. Analysis of white light interferograms using wavelet methods. *Optics Communications*, 1998, 148(1–3): 122–128
 106. Hart M, Vass D G, Begbie M L. Fast surface profiling by spectral analysis of white-light interferograms with Fourier transform spectroscopy. *Applied Optics*, 1998, 37(10): 1764–1769
 107. Freischlad K, Koliopoulos C L. Fourier description of digital phase-measuring interferometry. *Journal of the Optical Society of America. A, Optics and Image Science*, 1990, 7(4): 542–551
 108. Larkin K, Oreb B. Design and assessment of symmetrical phase-shifting algorithms. *Journal of the Optical Society of America. A, Optics and Image Science*, 1992, 9(10): 1740–1748
 109. de Groot P. Derivation of algorithms for phase-shifting interferometry using the concept of a data-sampling window. *Applied Optics*, 1995, 34(22): 4723–4730
 110. Schmit J, Creath K. Extended averaging technique for derivation of error-compensating algorithms in phase-shifting interferometry. *Applied Optics*, 1995, 34(19): 3610–3619
 111. Kumar U P, Bhaduri B, Kothiyal M, et al. Two-wavelength micro-interferometry for 3-D surface profiling. *Optics and Lasers in Engineering*, 2009, 47(2): 223–229
 112. Bankhead A D, McDonnell I. US Patent, 7385707, 2008-06-10
 113. Ai C, Novak E L. US Patent, 5633715, 1997-05-27
 114. Chen S, Palmer A, Grattan K, et al. Fringe order identification in optical fibre white-light interferometry using centroid algorithm method. *Electronics Letters*, 1992, 28(6): 553–555
 115. Alexander B F, Ng K C. Elimination of systematic error in subpixel accuracy centroid estimation. *Optical Engineering*, 1991, 30(9): 1320–1332
 116. Harasaki A, Wyant J C. Fringe modulation skewing effect in white-light vertical scanning interferometry. *Applied Optics*, 2000, 39(13): 2101–2106
 117. Suematsu M, Takeda M. Wavelength-shift interferometry for distance measurements using the Fourier transform technique for fringe analysis. *Applied Optics*, 1991, 30(28): 4046–4055
 118. Takeda M, Ina H, Kobayashi S. Fourier-transform method of fringe-pattern analysis for computer-based topography and interferometry. *Journal of the Optical Society of America*, 1982, 72(1): 156–160
 119. Takeda M, Mutoh K. Fourier transform profilometry for the automatic measurement of 3-D object shapes. *Applied Optics*, 1983, 22(24): 3977
 120. Su X, Chen W. Fourier transform profilometry: A review. *Optics and Lasers in Engineering*, 2001, 35(5): 263–284
 121. Chim S S, Kino G S. Correlation microscope. *Optics Letters*, 1990, 15(10): 579–581
 122. Chim S S, Kino G S. Phase measurements using the Mirau correlation microscope. *Applied Optics*, 1991, 30(16): 2197–2201
 123. Trusiak M, Wielgus M, Patorski K. Advanced processing of optical fringe patterns by automated selective reconstruction and enhanced fast empirical mode decomposition. *Optics and Lasers in Engineering*, 2014, 52: 230–240
 124. Huang L, Kemao Q, Pan B, et al. Comparison of Fourier transform, windowed Fourier transform, and wavelet transform methods for phase extraction from a single fringe pattern in fringe projection profilometry. *Optics and Lasers in Engineering*, 2010, 48(2): 141–148
 125. Kemao Q. Applications of windowed Fourier fringe analysis in optical measurement: A review. *Optics and Lasers in Engineering*, 2015, 66: 67–73
 126. Kemao Q. Two-dimensional windowed Fourier transform for fringe pattern analysis: Principles, applications and implementations. *Optics and Lasers in Engineering*, 2007, 45(2): 304–317
 127. Kemao Q, Wang H, Gao W. Windowed Fourier transform for fringe pattern analysis: Theoretical analyses. *Applied Optics*, 2008, 47(29): 5408–5419
 128. Kemao Q. Windowed Fourier transform for fringe pattern analysis. *Applied Optics*, 2004, 43(13): 2695–2702
 129. Zweig D A, Hufnagel R E. Hilbert transform algorithm for fringe-pattern analysis. *Proceedings of SPIE 1333, Advanced Optical Manufacturing and Testing*, 1990, 1333: 295–303
 130. Chim S S, Kino G S. Three-dimensional image realization in interference microscopy. *Applied Optics*, 1992, 31(14): 2550–2553
 131. Zhao Y, Chen Z, Ding Z, et al. Real-time phase-resolved functional optical coherence tomography by use of optical Hilbert transformation. *Optics Letters*, 2002, 27(2): 98–100
 132. Onodera R, Watanabe H, Ishii Y. Interferometric phase-measurement using a one-dimensional discrete Hilbert transform. *Optical Review*, 2005, 12(1): 29–36
 133. Li M, Quan C, Tay C. Continuous wavelet transform for micro-component profile measurement using vertical scanning interferometry. *Optics & Laser Technology*, 2008, 40(7): 920–929
 134. Li S, Su X, Chen W. Wavelet ridge techniques in optical fringe pattern analysis. *Journal of the Optical Society of America. A, Optics, Image Science, and Vision*, 2010, 27(6): 1245–1254
 135. Watkins L, Tan S, Barnes T. Determination of interferometer phase distributions by use of wavelets. *Optics Letters*, 1999, 24(13): 905–907
 136. Zhong J, Weng J. Phase retrieval of optical fringe patterns from the ridge of a wavelet transform. *Optics Letters*, 2005, 30(19): 2560–2562
 137. de Groot P J, Deck L L. Surface profiling by frequency-domain analysis of white light interferograms. *Proceedings of SPIE 2248, Optical Measurements and Sensors for the Process Industries*, 1994, 2248: 101–105
 138. de Groot P, Colonna de Lega X, Kramer J, et al. Determination of fringe order in white-light interference microscopy. *Applied Optics*, 2002, 41(22): 4571–4578
 139. de Groot P, Colonna de Lega X. Signal modeling for low-coherence height-scanning interference microscopy. *Applied Optics*, 2004, 43(25): 4821–4830

140. Zhang S. Recent progresses on real-time 3D shape measurement using digital fringe projection techniques. *Optics and Lasers in Engineering*, 2010, 48(2): 149–158
141. Hariharan P, Oreb B, Eiju T. Digital phase-shifting interferometry: A simple error-compensating phase calculation algorithm. *Applied Optics*, 1987, 26(13): 2504–2506
142. Sandoz P. An algorithm for profilometry by white-light phase-shifting interferometry. *Journal of Modern Optics*, 1996, 43(8): 1545–1554
143. de Groot P J. Long-wavelength laser diode interferometer for surface flatness measurement. *Proceedings of SPIE 2248, Optical Measurements and Sensors for the Process Industries*, 1994, 2248: 136–141
144. Dong Z, Chen Z. Advanced Fourier transform analysis method for phase retrieval from a single-shot spatial carrier fringe pattern. *Optics and Lasers in Engineering*, 2018, 107: 149–160
145. Ma S, Quan C, Zhu R, et al. Micro-profile measurement based on windowed Fourier transform in white-light scanning interferometry. *Optics Communications*, 2011, 284(10–11): 2488–2493
146. Ma S, Quan C, Zhu R, et al. Application of least-square estimation in white-light scanning interferometry. *Optics and Lasers in Engineering*, 2011, 49(7): 1012–1018
147. Zhang Z, Jing Z, Wang Z, et al. Comparison of Fourier transform, windowed Fourier transform, and wavelet transform methods for phase calculation at discontinuities in fringe projection profilometry. *Optics and Lasers in Engineering*, 2012, 50(8): 1152–1160
148. Huang J, Chen W, Su X. Application of two-dimensional wavelet transform in the modulation measurement profilometry. *Optical Engineering*, 2017, 56(3): 034105
149. Serizawa T, Suzuki T, Choi S, et al. 3-D surface profile measurement using spectral interferometry based on continuous wavelet transform. *Optics Communications*, 2017, 396: 216–220
150. de Groot P J. 101-frame algorithm for phase-shifting interferometry. *Proceedings of SPIE 3098, Optical Inspection and Micromasurements II*, 1997, 3098: 283–293
151. Shen M H, Hwang C H, Wang W C. Center wavelength measurement based on higher steps phase-shifting algorithms in white-light scanning interferometry. *Procedia Engineering*, 2014, 79: 447–455
152. Shen M H, Hwang C H, Wang W C. Using higher steps phase-shifting algorithms and linear least-squares fitting in white-light scanning interferometry. *Optics and Lasers in Engineering*, 2015, 66: 165–173
153. Sifuzzaman M, Islam M, Ali M. Application of wavelet transform and its advantages compared to Fourier transform. *Journal of Physiological Sciences*, 2009, 13: 121–134
154. Wei D, Xiao M, Yang P. Do we need all the frequency components of a fringe signal to obtain position information in a vertical scanning wideband interferometer? *Optics Communications*, 2019, 430: 234–237
155. Wei D, Aketagawa M. Automatic selection of frequency domain filter for interference fringe analysis in pulse-train interferometer. *Optics Communications*, 2018, 425: 113–117
156. Pavliček P, Michalek V. White-light interferometry—Envelope detection by Hilbert transform and influence of noise. *Optics and Lasers in Engineering*, 2012, 50(8): 1063–1068
157. Huang N E, Shen Z, Long S R, et al. The empirical mode decomposition and the Hilbert spectrum for nonlinear and non-stationary time series analysis. *Proceedings of the Royal Society of London Series A: Mathematical, Physical and Engineering Sciences*, 1998, 454(1971): 903–995
158. Trusiak M, Patorski K, Pokorski K. Hilbert-Huang processing for single-exposure two-dimensional grating interferometry. *Optics Express*, 2013, 21(23): 28359–28379
159. Trusiak M, Służewski Ł, Patorski K. Single shot fringe pattern phase demodulation using Hilbert-Huang transform aided by the principal component analysis. *Optics Express*, 2016, 24(4): 4221–4238
160. Trusiak M, Mico V, Garcia J, et al. Quantitative phase imaging by single-shot Hilbert-Huang phase microscopy. *Optics Letters*, 2016, 41(18): 4344–4347
161. Deepan B, Quan C, Tay C. Determination of phase derivatives from a single fringe pattern using Teager Hilbert Huang transform. *Optics Communications*, 2016, 359: 162–170
162. Trusiak M, Styk A, Patorski K. Hilbert-Huang transform based advanced Bessel fringe generation and demodulation for full-field vibration studies of specular reflection micro-objects. *Optics and Lasers in Engineering*, 2018, 110: 100–112
163. Deng J, Wu D, Wang K, et al. Precise phase retrieval under harsh conditions by constructing new connected interferograms. *Scientific Reports*, 2016, 6(1): 24416
164. Rajshekhar G, Rastogi P. Multiple signal classification technique for phase estimation from a fringe pattern. *Applied Optics*, 2012, 51(24): 5869–5875
165. Rajshekhar G, Rastogi P. Fringe demodulation using the two-dimensional phase differencing operator. *Optics Letters*, 2012, 37(20): 4278–4280
166. Vishnoi A, Ramaiah J, Rajshekhar G. Phase recovery method in digital holographic interferometry using high-resolution signal parameter estimation. *Applied Optics*, 2019, 58(6): 1485–1490
167. Feng S, Chen Q, Gu G, et al. Fringe pattern analysis using deep learning. *Advanced Photonics*, 2019, 1(2): 025001
168. Gomez C, Su R, de Groot P, et al. Noise reduction in coherence scanning interferometry for surface topography measurement. *Nanomanufacturing and Metrology*, 2020, 3(1): 68–76
169. Gdeisat M, Burton D, Lilley F, et al. Fast fringe pattern phase demodulation using FIR Hilbert transformers. *Optics Communications*, 2016, 359: 200–206
170. Zhong M, Chen F, Xiao C, et al. 3-D surface profilometry based on modulation measurement by applying wavelet transform method. *Optics and Lasers in Engineering*, 2017, 88: 243–254
171. Bernal O D, Seat H C, Zabit U, et al. Robust detection of non-regular interferometric fringes from a self-mixing displacement sensor using bi-wavelet transform. *IEEE Sensors Journal*, 2016, 16(22): 7903–7910
172. Rajshekhar G, Rastogi P. Phase estimation using a state-space approach based method. *Optics and Lasers in Engineering*, 2013, 51(8): 1004–1007
173. Gurov I, Volynsky M. Interference fringe analysis based on recurrence computational algorithms. *Optics and Lasers in Engineering*, 2012, 50(4): 514–521
174. Gao W, Huyen N T T, Loi H S, et al. Real-time 2D parallel

- windowed Fourier transform for fringe pattern analysis using graphics processing unit. *Optics Express*, 2009, 17(25): 23147–23152
175. Vishnoi A, Rajshekhar G. Rapid deformation analysis in digital holographic interferometry using graphics processing unit accelerated Wigner-Ville distribution. *Applied Optics*, 2019, 58(16): 4420–4424
 176. Ramaiah J, Ajithaprasad S, Rajshekhar G. Graphics processing unit assisted diffraction phase microscopy for fast non-destructive metrology. *Measurement Science & Technology*, 2019, 30(12): 125202
 177. Hariharan P. Phase-shifting interferometry: Minimization of systematic errors. *Optical Engineering*, 2000, 39(4): 967–970
 178. de Groot P J. Correlated errors in phase-shifting laser Fizeau interferometry. *Applied Optics*, 2014, 53(19): 4334–4342
 179. Kim Y, Hibino K, Sugita N, et al. Error-compensating phase-shifting algorithm for surface shape measurement of transparent plate using wavelength-tuning Fizeau interferometer. *Optics and Lasers in Engineering*, 2016, 86: 309–316
 180. Wang Z, Han B. Advanced iterative algorithm for phase extraction of randomly phase-shifted interferograms. *Optics Letters*, 2004, 29(14): 1671–1673
 181. Wang Z, Han B. Advanced iterative algorithm for randomly phase-shifted interferograms with intra- and inter-frame intensity variations. *Optics and Lasers in Engineering*, 2007, 45(2): 274–280
 182. Cai L, Liu Q, Yang X. Phase-shift extraction and wave-front reconstruction in phase-shifting interferometry with arbitrary phase steps. *Optics Letters*, 2003, 28(19): 1808–1810
 183. Cai L Z, Liu Q, Yang X L. Simultaneous digital correction of amplitude and phase errors of retrieved wave-front in phase-shifting interferometry with arbitrary phase shift errors. *Optics Communications*, 2004, 233(1–3): 21–26
 184. Gao P, Yao B L, Lindlein N, et al. Phase-shift extraction for generalized phase-shifting interferometry. *Optics Letters*, 2009, 34(22): 3553–3555
 185. Zhang X, Wang J, Zhang X, et al. Correction of phase-shifting error in wavelength scanning digital holographic microscopy. *Measurement Science and Technology*, 2018, 29(5): 055002
 186. Larkin K G. A self-calibrating phase-shifting algorithm based on the natural demodulation of two-dimensional fringe patterns. *Optics Express*, 2001, 9(5): 236–253
 187. Guo H, Yu Y, Chen M. Blind phase shift estimation in phase-shifting interferometry. *Journal of the Optical Society of America. A, Optics, Image Science, and Vision*, 2007, 24(1): 25–33
 188. Guo H. Blind self-calibrating algorithm for phase-shifting interferometry by use of cross-bispectrum. *Optics Express*, 2011, 19(8): 7807–7815
 189. Wang Y, Lu X, Liu Y, et al. Self-calibration phase-shifting algorithm with interferograms containing very few fringes based on Fourier domain estimation. *Optics Express*, 2017, 25(24): 29971–29982
 190. Cao S, Wang Y, Lu X, et al. Advanced spatial spectrum fitting algorithm for significantly improving the noise resistance ability of self-calibration phase shifting interferometry. *Optics and Lasers in Engineering*, 2019, 112: 170–181
 191. Ghim Y S, Rhee H G, Davies A, et al. 3D surface mapping of freeform optics using wavelength scanning lateral shearing interferometry. *Optics Express*, 2014, 22(5): 5098–5105
 192. Fuerschbach K, Thompson K P, Rolland J P. Interferometric measurement of a concave, ϕ -polynomial, Zernike mirror. *Optics Letters*, 2014, 39(1): 18–21
 193. Leong-Hoi A, Claveau R, Flury M, et al. Detection of defects in a transparent polymer with high resolution tomography using white light scanning interferometry and noise reduction. *Proceedings of SPIE 9528, Videometrics, Range Imaging, and Applications XIII*, 2015, 9528: 952807
 194. Zhou R, Edwards C, Arbabi A, et al. Detecting 20 nm wide defects in large area nanopatterns using optical interferometric microscopy. *Nano Letters*, 2013, 13(8): 3716–3721
 195. Guo T, Gu Y, Chen J, et al. Surface topography measurement based on color images processing in white light interferometry. *Proceedings of SPIE 9525, Optical Measurement Systems for Industrial Inspection IX*, 2015, 9525: 952511
 196. Servin M, Quiroga J A, Padilla M. Fringe Pattern Analysis for Optical Metrology: Theory, Algorithms, and Applications. Weinheim: John Wiley & Sons, 2014, 57–145
 197. Petrov N V, Skobnikov V A, Shevkunov I A, et al. Features of surface contouring by digital holographic interferometry with tilt of the object illumination. *Proceedings of SPIE 10749, Interferometry XIX*, 2018, 10749: 1074906
 198. Schmit J, Olszak A G. Challenges in white-light phase-shifting interferometry. *Proceedings of SPIE 4777, Interferometry XI: Techniques and Analysis*, 2002, 4777: 118–127
 199. Petzing J N, Coupland J M, Leach R K. The Measurement of Rough Surface Topography Using Coherence Scanning Interferometry. NPL Measurement Good Practice Guide 116. Middlesex: Queen's Printer and Controller of HMSO, 2010, 91–110
 200. Fay M F, Colonna de Lega X, de Groot P. Measuring high-slope and super-smooth optics with high-dynamic-range coherence scanning interferometry. In: *Proceedings of Optical Fabrication and Testing*. Hawaii: Optical Society of America, 2014, OW1B.3
 201. Marinello F, Bariani P, Pasquini A, et al. Increase of maximum detectable slope with optical profilers, through controlled tilting and image processing. *Measurement Science & Technology*, 2007, 18(2): 384–389
 202. de Groot P J. Vibration in phase-shifting interferometry. *Journal of the Optical Society of America. A, Optics, Image Science, and Vision*, 1995, 12(2): 354–365
 203. Wiersma J T, Wyant J C. Vibration insensitive extended range interference microscopy. *Applied Optics*, 2013, 52(24): 5957–5961
 204. Liu Q, Li L, Zhang H, et al. Simultaneous dual-wavelength phase-shifting interferometry for surface topography measurement. *Optics and Lasers in Engineering*, 2020, 124: 105813
 205. Li Y, Kästner M, Reithmeier E. Vibration-insensitive low coherence interferometer (LCI) for the measurement of technical surfaces. *Measurement*, 2017, 104: 36–42
 206. Liu Q, Huang W, Li L, et al. Vibration-resistant interferometric measurement of optical surface figure and roughness. *Proceedings of SPIE 11383, Sixth Asia Pacific Conference on Optics Manufacture*, 2020, 11383: 1138304

207. Colonna de Lega X, de Groot P. Lateral resolution and instrument transfer function as criteria for selecting surface metrology instruments. In: *Proceedings of Optical Fabrication and Testing*. Monterey: Optical Society of America, 2012, OTu1D.4
208. de Groot P, Colonna de Lega X, Sykora D, et al. The meaning and measure of lateral resolution for surface profiling interferometers. *Optics and Photonics News*, 2012, 23(4): 10–13
209. Indebetouw G, Tada Y, Rosen J, Brooker G. Scanning holographic microscopy with resolution exceeding the Rayleigh limit of the objective by superposition of off-axis holograms. *Applied Optics*, 2007, 46(6): 993–1000
210. Dong J, Jia S, Jiang C. Surface shape measurement by multi-illumination lensless Fourier transform digital holographic interferometry. *Optics Communications*, 2017, 402: 91–96
211. Merola F, Paturzo M, Coppola S, et al. Self-patterning of a polydimethylsiloxane microlens array on functionalized substrates and characterization by digital holography. *Journal of Micro-mechanics and Microengineering*, 2009, 19(12): 125006
212. Bray M. Stitching interferometer for large Plano optics using a standard interferometer. *Proceedings of SPIE 3134, Optical Manufacturing and Testing II*, 1997, 3134: 39–51
213. Otsubo M, Okada K, Tsujiuchi J. Measurement of large plane surface shapes by connecting small-aperture interferograms. *Optical Engineering*, 1994, 33(2): 608–613
214. Murphy P, Forbes G, Fleig J, et al. Stitching interferometry: A flexible solution for surface metrology. *Optics and Photonics News*, 2003, 14(5): 38–43
215. Fleig J, Dumas P, Murphy P E, et al. An automated subaperture stitching interferometer workstation for spherical and aspherical surfaces. *Proceedings of SPIE 5188, Advanced Characterization Techniques for Optics, Semiconductors, and Nanotechnologies*, 2003, 5188: 296–307
216. Dumas P R, Fleig J, Forbes G W, et al. Flexible polishing and metrology solutions for free-form optics. In: *Proceedings of the ASPE 2004 Winter Topical Meeting on Free-Form Optics: Design, Fabrication, Metrology, Assembly*. Glasgow: Citeseer, 2004, 1–6
217. Lei Z, Liu X, Zhao L, et al. A novel 3D stitching method for WLI based large range surface topography measurement. *Optics Communications*, 2016, 359: 435–447
218. Niehaus F, Huttenhuis S, Danger T. New opportunities in freeform manufacturing using a long stroke fast tool system and integrated metrology. *Proceedings of SPIE 9633, Optifab 2015*, 2015, 9633: 96331E
219. Lei W, Hsu Y. Accuracy enhancement of five-axis CNC machines through real-time error compensation. *International Journal of Machine Tools and Manufacture*, 2003, 43(9): 871–877
220. Yang J, Altintas Y. A generalized on-line estimation and control of five-axis contouring errors of CNC machine tools. *International Journal of Machine Tools and Manufacture*, 2015, 88: 9–23
221. Suh S H, Lee E S, Sohn J W. Enhancement of geometric accuracy via an intermediate geometrical feedback scheme. *Journal of Manufacturing Systems*, 1999, 18(1): 12–21
222. Ke Z, Yuen A, Altintas Y. Pre-compensation of contour errors in five-axis CNC machine tools. *International Journal of Machine Tools and Manufacture*, 2013, 74(8): 1–11
223. Gao W, Tano M, Sato S, et al. On-machine measurement of a cylindrical surface with sinusoidal micro-structures by an optical slope sensor. *Precision Engineering*, 2006, 30(3): 274–279
224. Gao W, Aoki J, Ju B F, et al. Surface profile measurement of a sinusoidal grid using an atomic force microscope on a diamond turning machine. *Precision Engineering*, 2007, 31(3): 304–309
225. Gao W, Chen Y L, Lee K W, et al. Precision tool setting for fabrication of a microstructure array. *CIRP Annals-Manufacturing Technology*, 2013, 62(1): 523–526
226. Zou X, Zhao X, Li G, et al. Non-contact on-machine measurement using a chromatic confocal probe for an ultra-precision turning machine. *International Journal of Advanced Manufacturing Technology*, 2017, 90(5–8): 2163–2172
227. Jiang X, Wang K, Martin H. Near common-path optical fiber interferometer for potentially fast on-line microscale-nanoscale surface measurement. *Optics Letters*, 2006, 31(24): 3603–3605
228. Li D, Tong Z, Jiang X, et al. Calibration of an interferometric on-machine probing system on an ultra-precision turning machine. *Measurement*, 2018, 118: 96–104
229. Li D, Jiang X, Tong Z, et al. Development and application of interferometric on-machine surface measurement for ultraprecision turning process. *Journal of Manufacturing Science and Engineering*, 2019, 141(1): 014502
230. Elkott D F, Veldhuis S C. Isoparametric line sampling for the inspection planning of sculptured surfaces. *Computer Aided Design*, 2005, 37(2): 189–200
231. He G, Sang Y, Pang K, et al. An improved adaptive sampling strategy for freeform surface inspection on CMM. *International Journal of Advanced Manufacturing Technology*, 2018, 96(1–4): 1521–1535
232. He G, Sang Y, Wang H, et al. A profile error evaluation method for freeform surface measured by sweep scanning on CMM. *Precision Engineering*, 2019, 56: 280–292
233. Babu M, Franciosa P, Ceglarek D. Adaptive measurement and modelling methodology for in-line 3D surface metrology scanners. *Procedia CIRP*, 2017, 60: 26–31
234. Babu M, Franciosa P, Ceglarek D. Spatio-temporal adaptive sampling for effective coverage measurement planning during quality inspection of free form surfaces using robotic 3D optical scanner. *Journal of Manufacturing Systems*, 2019, 53: 93–108
235. Chen Y, Peng C. Intelligent adaptive sampling guided by Gaussian process inference. *Measurement Science & Technology*, 2017, 28(10): 105005
236. Yin Y, Ren M J, Sun L, et al. Gaussian process based multi-scale modelling for precision measurement of complex surfaces. *CIRP Annals-Manufacturing Technology*, 2016, 65(1): 487–490
237. Yin Y, Ren M J, Sun L. Dependant Gaussian processes regression for intelligent sampling of freeform and structured surfaces. *CIRP Annals-Manufacturing Technology*, 2017, 66(1): 511–514
238. Gao W, Kemao Q. Parallel computing in experimental mechanics and optical measurement: A review. *Optics and Lasers in Engineering*, 2012, 50(4): 608–617
239. Wang T, Kemao Q. Parallel computing in experimental mechanics and optical measurement: A review (II). *Optics and Lasers in Engineering*, 2018, 104: 181–191
240. Karpinsky N, Zhang S. High-resolution, real-time 3D imaging with fringe analysis. *Journal of Real-Time Image Processing*, 2012,

- 7(1): 55–66
241. Van der Jeught S, Soons J A, Dirckx J J. Real-time microscopic phase-shifting profilometry. *Applied Optics*, 2015, 54(15): 4953–4959
242. Sinha A, Lee J, Li S, et al. Lensless computational imaging through deep learning. *Optica*, 2017, 4(9): 1117–1125
243. Rivenson Y, Göröcs Z, Günaydin H, et al. Deep learning microscopy. *Optica*, 2017, 4(11): 1437–1443
244. Rivenson Y, Zhang Y, Günaydin H, et al. Phase recovery and holographic image reconstruction using deep learning in neural networks. *Light, Science & Applications*, 2018, 7(2): 17141
245. Yin W, Chen Q, Feng S, et al. Temporal phase unwrapping using deep learning. *Scientific Reports*, 2019, 9(1): 1–12
246. Feng S, Zuo C, Yin W, et al. Micro deep learning profilometry for high-speed 3D surface imaging. *Optics and Lasers in Engineering*, 2019, 121: 416–427